Earth-Science Reviews 252 (2024) 104753

Contents lists available at ScienceDirect

Earth-Science Reviews

journal homepage: www.elsevier.com/locate/earscirev

On the prediction of the characteristics of sand ripples at the bottom of sea waves

Giovanna Vittori [*], Paolo Blondeaux

Department of Civil, Chemical and Environmental Engineering, University of Genoa, Via Montallegro 1, 16145 Genova, Italy

ARTICLE INFO

Keywords:
Wave ripples
Vortex structures
Sediment transport

ABSTRACT

In this review paper, the main geometrical characteristics of sea ripples (the smallest morphological patterns that are observed at the bottom of sea waves) are reviewed together with the physical mechanisms that give rise to their appearance and control their time development. Moreover, we provide a summary of both the mathematical tools (stability analyses) and empirical formulae that can be used to predict their appearance and some of their geometrical characteristics. The ripples play a relevant role in the mechanics of coastal sediment transport since usually the flow separates at the ripple crests and generates vortex structures that pick-up the sediments from the bottom and put them into suspension. Moreover, the vortex structures shed by the ripples significantly affect wave damping and flow resistance.

1. Introduction

Ripples are periodic morphological patterns that appear at the sea bottom and are characterized by a size of the order of tens of centimetres. These bedforms are generated and maintained by the interaction of the flowing sea water with cohesionless sediments (usually sand) that make up the bottom. Ripples are genetically similar to both sand waves and tidal ridges as well as river dunes and other morphological patterns observed along river (see a.o. Engelund and Fredsoe (1982), Garotta et al. (2006), Luchi et al. (2012), Bolla Pittaluga and Imran (2014)), since they are originated by the instability of the flat configuration of the bottom. This instability leads to the growth of bottom wavinesses of different lengths depending on the characteristics of both the sand and the water flow. There seems to be a continuum of bedforms from the smallest ripples (centimetres long) to the giant bedforms (kilometres long). Even though the ripples are the smallest bedforms, they play a prominent role in many transport processes since, usually, the flow separates at their crests and the vortices that are generated increase momentum transfer, sediment transport and, in general, mixing phenomena. Moreover, for high values of the bottom shear stress, the ripples are washed out and large amounts of sediment are put into suspension with significant effects on the fluxes of nutrients, oxigen and carbonates (Tengberg et al. (2003)).

As pointed out by Amos et al. (2019), the literature on ripples is immense since, after the first publication of Darwin (1883), new results are continuously produced and unavoidably it is not possible to mention all the contributions on this subject. Hereinafter, we try to provide an overview of the results that, in our opinion, are the most relevant.

Usually, ripples are classified into two main groups depending on the characteristics of the flow that originates them: current ripples and wave ripples. The former are originated by a steady current that drags the sediment in the flow direction, the latter are originated by the to and fro motion of the water produced close to the sea bottom by a propagating or standing surface wave. Hereinafter, we focus our attention on wave ripples since current ripples are dealt in Vittori and Blondeaux (2022). Even restricting our attention to wave ripples, different morphological patterns can be identified on the basis of their shape.

By analysing field data, Komar (1974) and Clifton and Dingler (1984) showed that the crest-to-crest distance of wave ripples either scales to the near-bed wave orbital diameter (orbital ripples) or to the grain size (anorbital ripples). In particular anorbital ripples appear when the ratio between the amplitude of the fluid oscillations close to the bottom and the sediment size d is very large and these bedforms are characterized by a wavelength which usually falls between $400d$ and $600d$ (a more precise value can not be given since field observations show a large scatter). At last, suborbital wave ripples are defined as a transition class between orbital and anorbital ripples and their wavelength depends both on the wave orbital diameter and the grain size. Attempts to predict the ripple characteristics from the knowledge of the sediment size and the wave orbital diameter have been made (Sleath (1984)) but a widely accepted approach does not exist yet.

---

[*] Corresponding author.
E-mail addresses: giovanna.vittori@unige.it (G. Vittori), paolo.blondeaux@unige.it (P. Blondeaux).

https://doi.org/10.1016/j.earscirev.2024.104753
Received 27 September 2023; Received in revised form 19 March 2024; Accepted 20 March 2024

Main symbols

A^*	any symbol with a star denotes the complex conjugate of the symbol (e.g. A^* is the complex conjugate of A)
a	amplitude of the sea wave
$A(t)$	dimensionless function of time describing the growth/decay of the amplitude of the bottom perturbation
$A_1(t), A_2(t), A_3(t)$	dimensionless function of time describing the growth/decay of the amplitude of the three components of the bottom perturbation
d	mean grain size
$\mathbf{D}$	symmetric part of the velocity gradient tensor
$D^* = \left[\frac{(s-1)gd^3}{\nu^2}\right]^{1/3} = R_p^{2/3}$	sediment diffusivity due to turbulence
$F_d = \frac{U_0}{\sqrt{(s-1)gd}} = \sqrt{\psi_d}$	sediment Froude number
g	gravitational acceleration
$Ga = R_p^2 = \frac{(s-1)gd^3}{\nu^2}$	Galileo number
h	mean water depth
h_r	ripple height
$i = \sqrt{-1}$	imaginary unit
J	Jacobian of the transformation (25)
$k = \frac{2\pi}{L}$	wavenumber of the sea wave
k_s	Nikuradse roughness
ℓ_1, ℓ_2	lengths of the down-current and up-current sides of the ripple
L	wavelength of the sea wave
n	bottom porosity
p	pressure
P	modified pressure that is equal to the pressure minus the hydrostatic contribution, i.e. $P = p + \rho g(z - \eta)$
p_{or}	porosity of the bottom material
(Q_x, Q_y)	horizontal components of the sediment transport rate per unit width
(Q_{Bx}, Q_{By})	horizontal components of the bed load sediment transport rate per unit width
(Q_{Px}, Q_{Py})	horizontal components of the sediment transport rate per unit width due to the bottom slope
(Q_{Sx}, Q_{Sy})	horizontal components of the suspended load sediment transport rate per unit width
$\widehat{r} = \frac{U_0}{\omega h_0}$	Keulegan number
$R_d = \frac{U_0 d}{\nu}$	Reynolds number of the sediment particle
$Re = \frac{U_0^2}{\nu\omega} = \frac{R_\delta^2}{2}$	flow Reynolds number
$R_\delta = \frac{U_0\delta}{\nu}$	flow Reynolds number
$R_p = \sqrt{(s-1)gd^3}\nu$	sediment Reynolds number
$s = \frac{\rho_s}{\rho}$	relative density
t	time coordinate
T	period of the sea waves
(u, v, w)	velocity components in the Cartesian coordinate system
u_s	steady velocity component just outside the bottom boundary layer
u_{slip}	slip velocity
u_τ	friction velocity
U_0	amplitude of the oscillations of the horizontal velocity component close to the bottom
w_s	sediment fall velocity
(x, y, z)	Cartesian coordinate system with the z^*-axis vertical and pointing upwards
z	vertical coordinate
z_{b0}	elevation of the flat bottom
z_r	bottom roughness
$\alpha = \frac{2\pi}{\lambda_r}$	wavenumber of a two-dimensional bottom perturbation
(α_x, α_y)	wavenumbers of the generic harmonic component of the bottom perturbation
$\delta = \sqrt{2\nu/\omega}$	thickness of the viscous bottom boundary layer
ϵ	dimensionless parameter much smaller than 1
η_s	free surface elevation
$\eta(x, y, t)$	bottom profile
Γ_r and Γ_i	real and imaginary parts of Γ. Γ_r determines the growth/decay of the bottom forms and Γ_i determines their migration speed
λ_r	ripple wavelength
μ_β	coefficient that determines the down-slope sediment transport rate
ν	kinematic viscosity of the water
ν_T	kinematic eddy viscosity
ψ	stream function such that $\frac{\partial\psi}{\partial x} = u$ and $-\frac{\partial\psi}{\partial y} = v$
$\psi_d = \frac{U_0^2}{(s-1)gd}$	sediment mobility number
ρ, ρ_s	densities of the water and of the sediment grains, respectively
η_r	height of the ripples
(τ_x, τ_y)	horizontal components of the bottom shear stress
$\tau = \sqrt{\tau_x^2 + \tau_y^2}$	bottom shear stress
θ	Shields parameter
θ_{crit}	critical value of the Shields parameter for the inception of sediment transport
ζ	reference level to impose the bottom boundary condition for the sediment concentration
$\omega = \frac{2\pi}{T}$	angular frequency of the sea waves
Ω	vorticity
$\mathbf{O}$	antisymmetric part of the velocity gradient tensor

Recent field observations show that bedforms characterized by different length scales might occur simultaneously. For example, Hanes et al. (2001) observed a clear bimodal distribution of ripple wavelength with two peaks, one for short wave ripples (SWR), characterized by a wavelegth smaller than 0.35 m, and one for long wave ripples (LWR), characterized by a wavelength longer than 0.5 m. The bimodality suggest that either SWR and LWR have different formation mechanisms (Boyd et al. (1988), Hanes et al. (2001), Grasmeijer (2002)) or the appearance of these bedforms is simply due to the growth of different unstable modes. It is not uncommon to observe both two-dimensional and three-dimensional ripples (see for example the book of Sleath (1984)) as well as regular and irregular bottom profiles. However, in the modelling of large scale phenomena, wave ripples are often considered just as a bottom roughness, the size of which depends on the height and length of the bottom forms but not on their planform.

Since we share the opinion expressed by De Vriend (2001) that the research on morphodynamics should be based on i) field and laboratory observations, ii) theoretical investigations and iii) numerical studies, in the following we describe both field and laboratory data and make a brief overwiev of the theoretical analyses as well as of the numerical investigations, which are a powerful tool to obtain a detailed picture of a phenomenon but still need the formulation of 'ad hoc' models and a careful verification of the results using the experimental measurements. The aim of this paper is to make an overview of the tools available to predict the appearance of ripples on the sea bottom and to determine their main geometrical characteristics. Indeed sea ripples have different shapes, lengths and heights which depend on the characteristics of both the surface waves and the steady currents which generate them. In the past, review papers appeared (Southard (1991), Blondeaux (2001)) describing the characteristics of the ripples appearing on the sea bottom. However, Southard (1991) describes the bed configurations generated by both steady and oscillatory flows and classifies them using different diagrams but on the basis of experimental measurements only. Blondeaux (2001) considered all the bedforms which appear in the coastal area, i.e. tidal ridges, sand waves, sand ridged, shoreface-connected ridges, longshore bars, crescentic forms, welded bars, beach cusps, ripples, thus dedicating little space to the analysis of ripple characteristics.

Let us point out that, since the manuscript was aimed at describing the predictive tools able to determine ripple characteristics as function of surface wave and sediment characteristics, we did not review the papers describing field measurements but we limit ourselves to use field data when strictly necessary to support the theoretical predictions.

2. The mechanism of ripple formation

Wave ripples are generated by steady recirculating cells that, in turn, are generated by the interaction of the oscillatory flow, induced by surface waves close to the bottom, with a bottom waviness of small amplitude. Indeed, a flat sea bottom is always characterized by the presence of small perturbations that can be considered as the superposition of different Fourier modes that, because of their small amplitude, affect the flow field independently of each other.

The sinusoidal bottom waviness forces a periodic spatial variation of the oscillatory flow. Then, the flow field due the interaction of the oscillating flow with the wavy bottom gives rise to a steady velocity component.

Fig. 1 shows an example of the flow visualizations of the steady velocity component made by Kaneko and Honji (1979). According to Kaneko and Honji (1979), if the ratio between the wavelength of the wall waviness and the thickness of oscillatory viscous wall layer (Stokes layer) is larger than about 26, the steady streaming has a double structure that consists of upper and lower pairs of recirculating cells. As the ratio between the amplitude of the wall waviness and the thickness of Stokes layer increases, the upper pair of recirculating cells squeezes in a gap between the lower pair just above the troughs of the wall. The shape and strength of the steady streamings depend on the parameters of the problem, namely, 1) the ratio h_r/λ_r between the height h_r and length λ_r of the bottom waviness, 2) the ratio $U_0/(\omega\lambda_r)$ between the amplitude U_0/ω of the fluid oscillations and λ_r (U_0 and $\omega = \frac{2\pi}{T}$ denote the amplitude and angular frequency of the velocity oscillations of the fluid particles, respectively), 3) the ratio between U_0/ω and the viscous length $\delta = \sqrt{2\nu/\omega}$ which is the order of magnitude of the thickness of the bottom boundary layer. Note that $U_0/(\omega\delta)$ is equal to $R_\delta/2$, $R_\delta = U_0\delta/\nu$ being the Reynolds number characteristic of the bottom boundary layer. As the values of these parameters change, different balances take place into momentum equation among the local acceleration term, the convective acceleration term, the pressure gradient term and the viscous term and different approaches must be used to determine the flow field. (see among others Lyne (1971), Sleath (1984), Vittori (1989), Blondeaux (1990)).

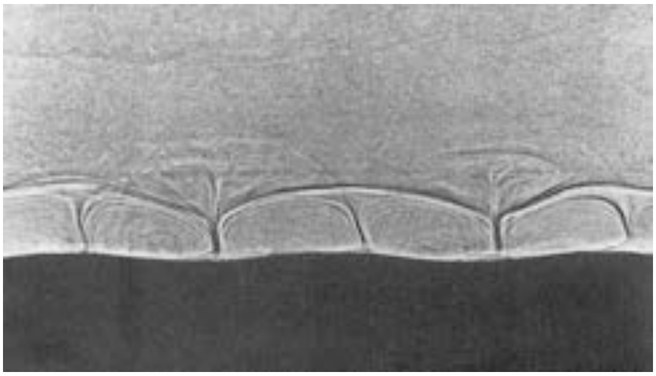

Fig. 1. Visualization of the flow patterns observed by Kaneko and Honji (1979) for 1) the ratio between the wavelength of the wall waviness and the thickness δ (defined in the text) of the viscous oscillatory boundary layer equal to 24 and 2) the ratio between the height of the wall waviness and δ equal to 0.92 (adapted from Journal of Fluid Mechanics).

If the steady velocity component near to the bottom points from the troughs towards the crests of the bottom waviness and is strong enough to move the sediments, the sediment particles tend to move from the troughs towards the crests. The tendency of the sediment particles to pile up at the crests of the bottom waviness is opposed by the gravity force component acting in the down-slope direction that generates a down-slope sediment flux. Hence, the growth of the bottom waviness is controlled by a balance between these two opposite effects. When gravity prevails over drag, the amplitude of the waviness decays, otherwise the amplitude grows leading to the appearance of ripples. Once formed, the ripples do not continue to grow because the steady streaming is modified by nonlinear effects and, as the ripples get steeper, an equilibrium configuration is attained.

3. Empirical formulae to predict the length and height of the ripples

Since laboratory and field data are important to identify and classify the morphological patterns that are present in the coastal region, let us start by providing a brief overview of the actual knowledge of ripples that is available on the basis of laboratory and field data.

As already pointed out, the geometry of sea ripples is often assumed to be two-dimensional and their profile to be similar to that of a wind wave, being characterized by crests and troughs (see the top panel of Fig. 2). However, the wavelength λ_r of the ripples is much smaller than the length of the wind waves, being of the order of magnitude of the amplitude of the fluid displacement oscillations induced close to the sea bottom by the wind waves, i.e. being of $O(10\ \mathrm{cm})$. Moreover, the ripples are only a few centimetres high. Similar values of the length and height of the ripples characterize also the three-dimensional ripples (see the bottom panel of Fig. 2).

The prediction of the length and height of the sea ripples is quite important because the ripple geometry affects the local flow field and the sediment transport. When the ratio between the height and the length of the ripples is smaller than a threshold value that Sleath (1984) suggests to be about 0.1, the boundary layer generated close to the bottom by the no-slip condition keeps attached to the bottom profile and the sediments roll and slide along the bottom. Hence, these ripples are named ‘rolling-grain’ ripples. On the other hand, when the ratio between the height and the length of the ripples becomes larger than 0.1, the flow separates from the crests of the bedforms and a vortex or more vortices are generated during each half cycle, being clockwise or counter-clockwise rotating depending on the direction of the free stream velocity. These vortices pick-up a lot of sediments from the bottom and later, when the flow reverses its direction, they are no longer reinforced and are simply convected by the free stream, dragging a lot of sediments along their trajectory. Later, the vortices decay because of viscous effects and the sediments settle down. In this case the ripples are named ‘vortex ripples’.

For practical purposes, the ripple length and height are usually predicted by means of empirical formulae. It is reasonble to assume that the ripple geometry depends on i) the density ρ of the sea water, ii) the kinematic viscosity of the sea water, iii) the period T of the fluid oscillations induced by surface waves close to the bottom or, alternatively, the angular frequency $\omega = 2\pi/T$, iv) the value U_0 of the amplitude of the velocity oscillations ($U_0 = a\omega/sinh(kh)$, where $k = 2\pi/L$ is the wave-

Fig. 2. Top panel: sand ripples on a beach near Sestroretsk, a suburb of Saint Petersburg, Russia, May 19, 2011. Bottom panel: rippled texture of a sandy bar at low tide along French Beach, Qatar, March 4, 2010 (courtesy of Alexey Sergeev).

number of the sea wave, *a* is its amplitude and *h* is the local water depth), v) the size *d* of the sediments, vi) the density ρ_s of the sediments and vii) the gravity acceleration *g*. Then, a dimensional analysis shows that the wavelength and height of the ripples depend on four dimensionless parameters, i.e. the ratio $s = \frac{\rho_s}{\rho}$ between the sediment and water densities, the ratio $\frac{d}{\delta}$ between the size of the sediment and the thickness δ of the viscous bottom boundary layer, the sediment Reynolds number $R_p = \frac{\sqrt{(s-1)gd^3}}{\nu}$ and the flow Reynolds number $R_\delta = \frac{U_0\delta}{\nu}$. Of course, these parameters can be replaced by any combination of them and in the literature it is common to encounter the mobility number $\psi_d = \frac{U_0^2}{(s-1)gd} = \left(\frac{R_\delta}{R_p}\frac{d}{\delta}\right)^2$, the sediment Froude number $F_d = \frac{U_0}{\sqrt{(s-1)gd}} = \sqrt{\psi_d}$, the Reynolds number R_d of the sediment particle defined by $R_d = \frac{U_0 d}{\nu} = R_p\sqrt{\psi}$, the Galilei number $Ga = \frac{(s-1)gd^3}{\nu^2} = R_p^2$, the flow Reynolds number $Re = \frac{U_0^2}{\nu\omega} = \frac{R_\delta^2}{2}$ and the parameter $D^* = \left(\frac{(s-1)gd^3}{\nu^2}\right)^{\frac{1}{3}} = R_p^{\frac{2}{3}}$.

These simple dimensional arguments show that ripple characteristics can not be predicted by means of just one paramenter. However, in the literature, the empirical formulae make use of only one parameter to make it simpler their use. Therefore, the first problem to be tackled is: which is the dimensionless parameter that mainly controls the geometrical characteristics of the ripples?

The plethora of empirical formulae that use different parameters and the significant differences among the values they provide seem to suggest that the problem of predicting ripple characteristics is far from a widely accepted solution. Some of the predictors, which are commonly used, are described and discussed in Nelson et al. (2013). In the following we provide a summary of the actual knowledge.

3.1. Ripple wavelength

Looking at field and laboratory data, the wavelengths of the ripples generated by regular surface waves appear to be somewhat different from the wavelengths of the ripples generated by random sea waves. Notwithstanding this experimental evidence, Soulsby and Whitehouse (2005), Nelson et al. (2013) and other authors proposed a single predictor for both regular and random waves. In particular, Soulsby and Whitehouse (2005) proposed to relate the ratio between the ripple wavelength λ_r and the amplitude U_0/ω of the fluid displacement oscillations close to the bottom to the dimensionless parameter $\frac{U_0}{\omega d}$:

$$\frac{\lambda_r}{U_0/\omega} = \frac{1}{a_1 + b_1\frac{U_0}{\omega d}\left[1 - e^{-\left(c_1\frac{U_0}{\omega d}\right)^{d_1}}\right]} \tag{1}$$

where

$$a_1 = 1, \qquad b_1 = 1.87\times10^{-3}, \qquad c_1 = 2.0\times10^{-4}, \qquad d_1 = 1.5 \tag{2}$$

Also Nelson et al. (2013) proposed to use (1) but the values of the constants they suggested are

$$a_1 = 0.72, \qquad b_1 = 2.00\times10^{-3}, \qquad c_1 = 1.57\times10^{-4}, \qquad d_1 = 1.15 \tag{3}$$

Fig. 3 shows a comparison between the observed ripple wavelengths and the empirical predictors of Soulsby and Whitehouse (2005) and Nelson et al. (2013).

In Fig. 3, the blue points are the wavelengths of the ripples generated by regular waves while the red points are the wavelengths of the ripples generated by random waves, the characteristics of which are determined using (1) and considering the significant wave height. Both data sets (regular waves and random waves) are extracted from the database collected by Nelson et al. (2013). The laboratory data obtained by means of an oscillating tray were not shown in Fig. 3 because Miller and Komar (1980) pointed out that the results obtained by oscillating the sediment bed are different from those obtained in water tunnels, wave channels and in the field. Moreover, not all the data of Nelson et al. (2013) are plotted in Fig. 3 because some of the data deviate significantly from the other data or refer to relic ripples, the characteristics of which can not be correlated to the actual hydrodynamic parameters. Notwithstanding this

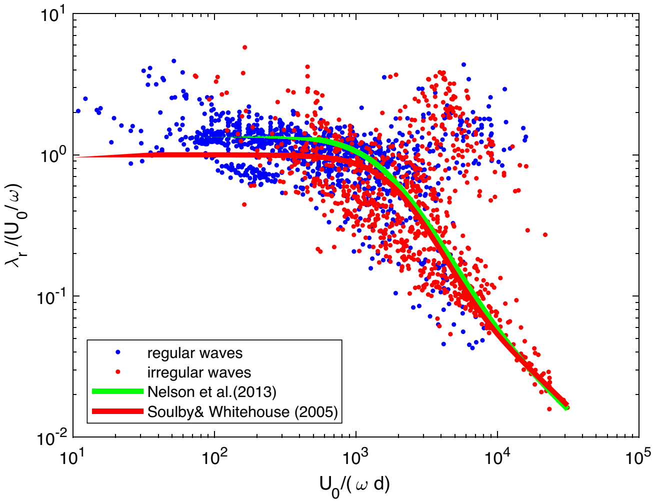

Fig. 3. Comparison between predicted (lines) and observed (points) ripple wavelengths. The experimental data are some of those collected by Nelson et al. (2013).

selection of the data, there is a small group of data that deviates from the trend of the empirical predictors.

On the basis of experimental data, Inman (1957) suggested that the ripple wavelength depends on the ratio $\frac{2U_0}{\omega}$ but it has different behaviours. The wavelength of the bedforms is proportional to the ratio $\frac{2U_0}{\omega}$ up to a threshold value whereupon some of the data show that the ripple wavelength keeps increasing with $\frac{2U_0}{\omega}$ but other data indicate that eventually the wavelength of the ripples attains a constant value.

Later, Clifton (1987) divided the ripples into three groups: orbital, anorbital and suborbital ripples. Orbital ripples have a wavelength that is proportional to the amplitude of the fluid displacement oscillations close to the bottom

$$\lambda_r \simeq 0.65\frac{2U_0}{\omega} \tag{4}$$

Anorbital ripples, which appear for large values of the ratio $\frac{2U_0/\omega}{d}$, have a wavelength which is almost independent of $\frac{2U_0}{\omega}$ and is proportional to the grain size, ranging between $400d$ and $600d$ (the large scatter of the data does not allow to give a more precise value).Moreover, suborbital ripples exist too and their wavelength depends on both $2U_0/\omega$ and the grain size d.

To show these different behaviours of the ripple wavelength, the top panel of Fig. 4 shows the ratio λ_r/d plotted versus the dimensionless parameter $(2U_0/\omega)/d$. Because, during the revision process, one reviewer pointed out that the use of dimensionless variables might obscure the genuine scatter of the observed values of the ripple wavelength, the bottom panel shows the wavelength of the ripples plotted versus twice the amplitude of the fluid displacement oscillations using dimensional variables.

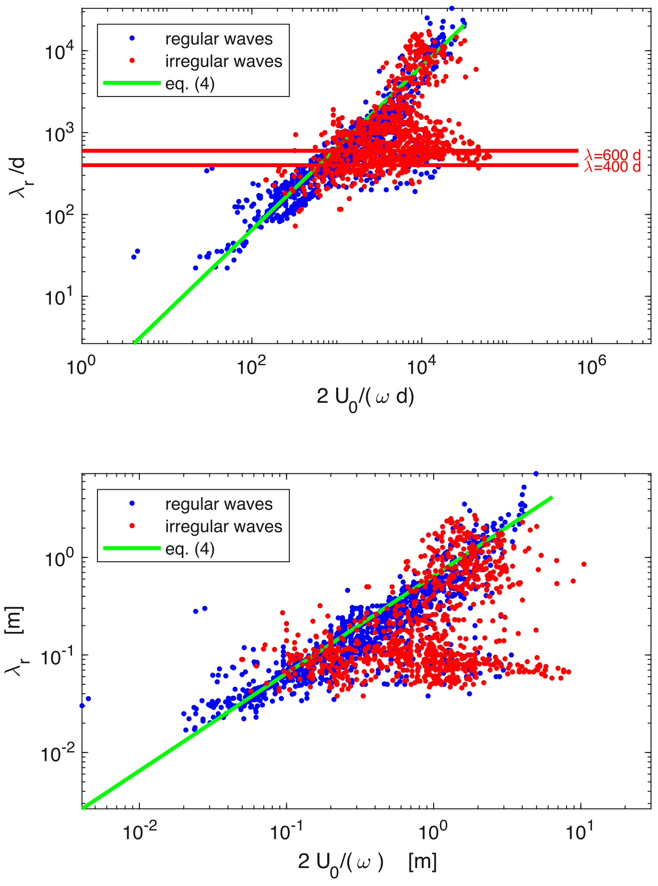

Fig. 4. Comparison between predicted (lines) and observed (points) ripple wavelengths. The experimental data are some of those collected by Nelson et al. (2013). In the top panel both the ripple wavelength and the amplitude of the fluid displacement oscillations are made dimensionless using the grain size d whereas in the bottom panel the dimensional values are used.

Nielsen (1981) proposed to predict the wavelength of the ripples by using the sediment mobility number ψ_d and he suggested to use

$$\frac{\lambda_r}{U_0/\omega} = exp\left(\frac{693-0.37ln^8\psi_d}{1000+0.75ln^7\psi_d}\right) \tag{5}$$

to predict the wavelength of the ripples observed in the field and

$$\frac{\lambda_r}{U_0/\omega} = 2.2-0.345\psi_d^{0.34} \tag{6}$$

to predict the wavelength of the ripples generated by a regular oscillatory flow. Fig. 5 shows the relationships (5) and (6) along with the measured ripple wavelength.

3.1.1. *Ripple height*

If the wavelength λ_r of the ripples is known, their height h_r can be obtained by means of the empirical formulae that provide the ripple steepness h_r/λ_r. Soulsby and Whitehouse (2005) suggest to use the following formula

$$\frac{h_r}{\lambda_r} = 0.15\left\{1-exp\left[-\left(\frac{5.0\times10^3 d}{(U_0/\omega)}\right)^{3.5}\right]\right\} \tag{7}$$

that predicts the ripple steepness h_r/λ_r as function of the ratio $\frac{U_0/\omega}{d}$.

Nelson et al. (2013) suggest to predict the ripple steepness as function of the ripple wavelength according to the formula $\frac{h_r}{\lambda_r} = 0.12\lambda_r^{-0.056}$ where λ_r should be in metres. The disavantage of Nelson et al.'s formula is that the ratio h_r/λ_r is given as function of a dimensional quantity. Fig. 6 shows a comparison between the results provided by (7) and the experimental measurements for both regular and and irregular waves.

3.1.2. *Ripple symmetry index*

The ripple profile is not symmetric with respect to its crests because a small degree of asymmetry is generated by both the weak steady velocity component, which is present under propagating sea wave (Longuet-Higgins (1953)), and by the difference between the forward velocity generated by the passage of the crests of the surface waves and the backward velocity generated by the passage of the troughs. Of course the asymmetry increases when a steady current is present.

The symmetry index is usually defined as the ratio of the length l_2 of

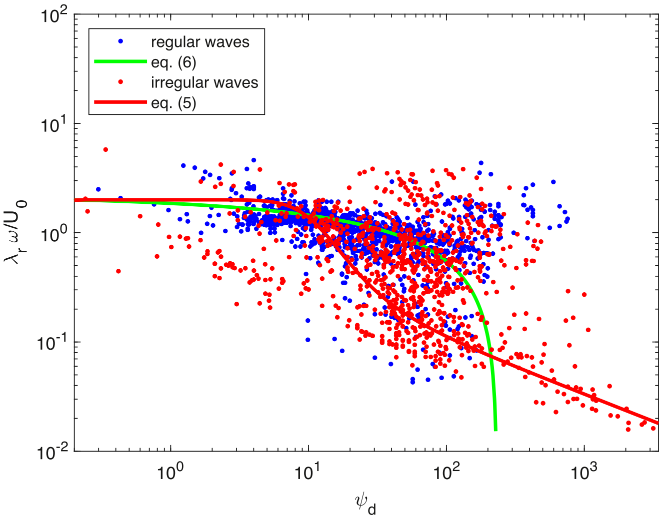

Fig. 5. Comparison between predicted (lines) and observed (points) ripple wavelengths. The experimental data are some of those collected by Nelson et al. (2013).

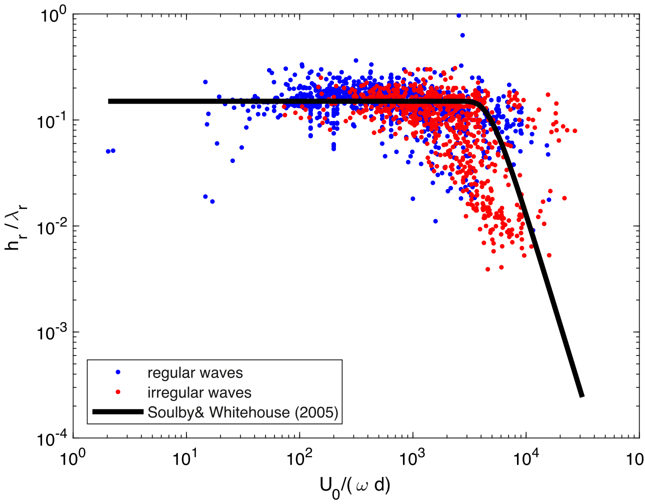

Fig. 6. Comparison between predicted (line) and observed (points) ripple steepnesses. The experimental data are some of those collected by Nelson et al. (2013).

the gentle (up-current) side to the length l_1 of the steep (down-current) side of the bottom forms. The experimental values of $\frac{l_2}{l_1}$ are plotted versus the strength of the steady current in Fig. 7 by considering the data of Inman (1957), Tanner (1971), Harms (1969), Tietze (1979), Inman and Bowen (1962) and Blondeaux et al. (2000). In the figure, when surface waves are considered, the steady velocity component u_s is evaluated by means of the theory of Longuet-Higgins (1953), i.e. $u_s = \frac{3\pi a^2\omega}{2L\sinh(2\pi h/L)}$. As expected, the results suggest that ripples tend to become more asymmetric as the mass transport velocity increases but with an asymptote for $\frac{l_2}{l_1}$ equal to about 2.5.

4. Idealized models of ripple appearance and dynamics

4.1. The appearance of rolling-grain ripples for moderate values of the Reynolds number

The mechanism that originates wave ripples is qualitatively understood since Sleath (1976) studied the oscillatory flow over a wavy wall and showed that a small bottom waviness interacting with an oscillatory flow induces a steady streaming that is superimposed on the basic oscillatory fluid motion and consists of recirculating cells the characteristics (form, intensity and direction) of which depend on the characteristics of the oscillatory flow and those of the wall waviness.

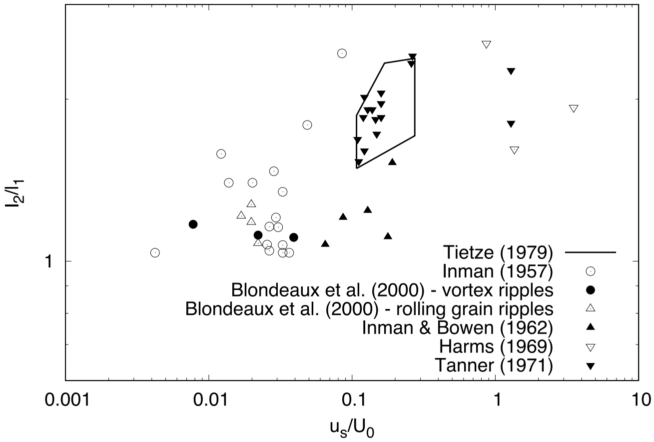

Fig. 7. Symmetry index, i.e. ratio between the length l_2 of the up-current side to the length l_1 of the down-current side of the ripples, plotted versus u_s/U_0 (u_s being the steady velocity component just outside the bottom boundary layer).

As pointed out in Section 2, when the steady velocity component close to the bottom is directed from the troughs towards the crests of the initial bottom waviness and is strong enough to drag the sediments, the sediments tend to move from the troughs towards the crests. The tendency of sediments to pile up near the crests is opposed by the component of the gravity force acting along the down-slope direction. Hence, the time development of the amplitude of the bottom waviness is controlled by a balance between these two effects. If gravity prevails over drag, the amplitude decays. On the other hand, if drag prevails on gravity, the amplitude grows leading to the appearance of ripples. Once formed, ripples do not continue to grow indefinitely because the steady streaming is modified by the nonlinear effects due to the interaction of the perturbation (induced by the bottom waviness) with itself. This self-induced interaction, which takes place because of the nonlinear convective terms of momentum equation, is not taken into account by a linear approach because the assumption of a small (strictly infinitesimal) amplitude of the perturbation leads to neglect nonlinear effects. Then, as ripples get steeper because their amplitude grows, an equilibrium configuration is attained which is controlled by nonlinear effects.

Sleath (1976) investigated the phenomenon by analytical means and considered two limiting cases, i.e. amplitudes of the fluid displacement oscillations either much larger or much smaller than the wavelength of the bottom waviness. Blondeaux (1990) determined the time development of a bottom waviness when the fluid displacement oscillations are of the same order of magnitude as the wavelength of the bottom waviness, as it is observed in the field.

In particular Blondeaux (1990) considered a two-dimensional wavy bottom described by

$$y = \eta(x,t) = \epsilon A(t)e^{i\alpha x} + c.c. \tag{8}$$

where the wavenumber α of the bottom waviness is related to λ_r by $\alpha = \frac{2\pi}{\lambda_r}$ and (x,y) is a fixed coordinate system with the x-axis coincident with the averaged bottom and aligned with the fluid oscillations and the y-axis is orthogonal to the bottom and points upwards.

Blondeaux (1990) considered the flow generated close to the bottom by a monochromatic surface wave for moderate values of the Reynolds number, such that the flow regime is laminar. When the bottom is flat, the flow is described by the well known Stokes' solution and far from the bottom, the fluid velocity oscillates with an amplitude U_0.

Then, it is useful to introduce a reference frame $(\widetilde{x},\widetilde{y})$ moving with the fluid far from the bottom, such that $\widetilde{x} = x + \frac{U_0}{2}\int_0^t \left(e^{i\omega t} + c.c.\right)dt$ and $\widetilde{y} = y$. Since the flow is two-dimensional, it is possible to introduce the stream function $\widetilde{\psi}$, such that $(\widetilde{u},\widetilde{v}) = \left(\frac{\partial\widetilde{\psi}}{\partial\widetilde{y}}, -\frac{\partial\widetilde{\psi}}{\partial\widetilde{x}}\right)$. Considering a bottom waviness of small amplitude ($\epsilon \ll 1$), it is possible to expand the stream function in the form

$$\widetilde{\psi} = \widetilde{\psi}_0 + \epsilon A(t)\left[\widetilde{\psi}_1 e^{i\alpha\widetilde{x}} + c.c.\right] + O\left(\epsilon^2\right) \tag{9}$$

The equation that provides the spanwise component of the vorticity, which is equal to $-\left(\frac{\partial^2\widetilde{\psi}}{\partial\widetilde{x}^2} + \frac{\partial^2\widetilde{\psi}}{\partial\widetilde{y}^2}\right)$, can be easily obtained by cross-differentiating the momentum equations along the $\widetilde{x}$- and $\widetilde{y}$-axes. By substituting (9) into vorticity equation, at order ϵ, it is easy to obtain

$$\frac{\partial}{\partial t}\left(N^2\widetilde{\psi}_1\right) + \frac{\partial\widetilde{\psi}_0}{\partial\widetilde{y}}N^2\widetilde{\psi}_1 - \frac{\partial^3\widetilde{\psi}_0}{\partial\widetilde{y}^3}\widetilde{\psi}_1 = \nu N^2\left(N^2\widetilde{\psi}_1\right) \tag{10}$$

where $N^2 = \frac{\partial^2}{\partial\widetilde{y}^2} - \alpha^2$. In (10) the term proportional to dA/dt is neglected because it describes the changes of A that take place on the morphodynamic temporal scale that is much longer than the wave period. Lastly, the no-slip condition at the bottom and the matching of the solution with the vanishing velocity far from the bottom close the problem.

Blondeaux (1990) determined the flow field by writing the solution of (10) in the form

$$\widetilde{\psi}_1 = \sum_{m=-\infty}^{\infty} G_m(\widetilde{y}) e^{im\omega t} \tag{11}$$

and obtaining the functions G_m as a double series of exponential functions of y (details of the solution procedure can be found in Blondeaux (1990)). The unavoidable presence in (11) of the term $G_0(\widetilde{y})$ shows that a steady streaming is generated by the interaction of the oscillatory flow with the bottom waviness. Fig. 8 shows examples of the streamlines related to the steady streaming generated by the fluid oscillations over a wavy wall of small amplitude, the wavelength of which is about 15δ for panel *a* and about 40δ for panel *b*. The results clearly show that 2 or 4 recirculating cells appear depending on the parameters of the hydrodynamic problem (Vittori (1989)).

Once the flow field is obtained, the time development of the waviness of the bottom can be determined by considering sediment continuity equation (Exner equation)

$$\frac{\partial \eta}{\partial t} = -\frac{1}{(1-p_{or})} \frac{\partial Q_x}{\partial x} \tag{12}$$

and by introducing a sediment transport predictor to evaluate the sediment transport rate Q_x per unit width (in (12) p_{or} denotes the bottom porosity). Since the flow is assumed to be laminar, the empirical formulae, commonly used, do not provide reliable estimates of the amount of sediment moved by the flow, because they are designed to quantify the sediment transport rate when the flow regime is turbulent and the sediment dynamics is largely affected by the turbulent eddies. Hence, Blondeaux (1990) used a modified version of the formula proposed by Grass and Ayoub (1982). A term proportional to the local bottom slope was introduced by Blondeaux (1990) into the sediment transport predictor to take into account the effects that the bottom slope has on the sediment transport rate.

Sediment continuity Eq. (12) leads to an equation which can be written in the form

$$\frac{dA}{d(\omega t)} = \Gamma(\omega t) A(\omega t) \tag{13}$$

where the function $\Gamma(\omega t)$, which turns out to be complex ($\Gamma = \Gamma_r + i\Gamma_i$), depends on the oscillatory flow over the wavy bottom or, in other words, on the solution of (10) and on the sediment transport rate at the same order of approximation (see Blondeaux (1990)). The solution of Eq. (13) reads $A(\omega t) = A_0 e^{\int \Gamma(\omega t) d(\omega t)} = A_0 e^{(\overline{\Gamma}_r + i\overline{\Gamma}_i)\omega t} e^{\int [(\Gamma_r - \overline{\Gamma}_r) + i(\Gamma_i - \overline{\Gamma}_i)] d(\omega t)}$ where the time average $\overline{\Gamma}_r$ of Γ_r describes the growth/decay of the bottom waviness, depending on its positive/negative value, and the time average $\overline{\Gamma}_i$ of Γ_i is related to the migration speed of the bottom forms. Because of the symmetry of the problem, $\overline{\Gamma}_i$ and the average migration speed vanish. The periodic parts of Γ, characterized by a vanishing time average (namely $\Gamma_r - \overline{\Gamma}_r$ and $\Gamma_i - \overline{\Gamma}_i$), turn out to be small and describe the vertical and horizontal small oscillations of the bottom profile taking place during the wave cycle.

Two contributions to $\overline{\Gamma}_r$ can be indentified. One contribution turns out to be positive (destabilizing) and is due to the sediments moving from the troughs towards the crests of the bottom waviness driven by the steady streamings. The second contribution, which is due to the bottom slope, is negative and has a stabilizing effect, since it is due to the sediments that move from the crests towards the troughs of the bottom waviness because of gravity effects. Therefore, the behaviour of the bottom waviness is controlled by a balance between these two effects. Fig. 9 shows $\overline{\Gamma}_r$ as function of α for different values of ψ_d and for fixed values of the other flow and sediment parameters. Looking at Fig. 9, it appears that a critical value $\psi_{d,crit}$ of the mobility number ψ_d exists such that for values of ψ_d larger than the critical value, perturbation components characterized by wavenumbers falling within a restricted range around a critical wavenumber α_{crit} grow exponentially in time. A larger value of ψ_d leads to an increase of the range of unstable wavenumbers (wavenumbers with a positive growth rate) while a decrease of ψ_d makes the unstable wavenumbers to collapse around α_{crit}. A change of the parameters of the problem leads to quantitative changes of the results but no qualitative change is observed. If the critical values of α are plotted versus R_δ for different values of R_d, it can be observed that coarser sediments, which are characterized by higher values of R_d, give rise to longer ripples. Fig. 10 shows α_{crit} as function of R_δ for different values of R_d, along with the experimental measurements of Blondeaux et al. (1988). The comparison between the theoretical values and the

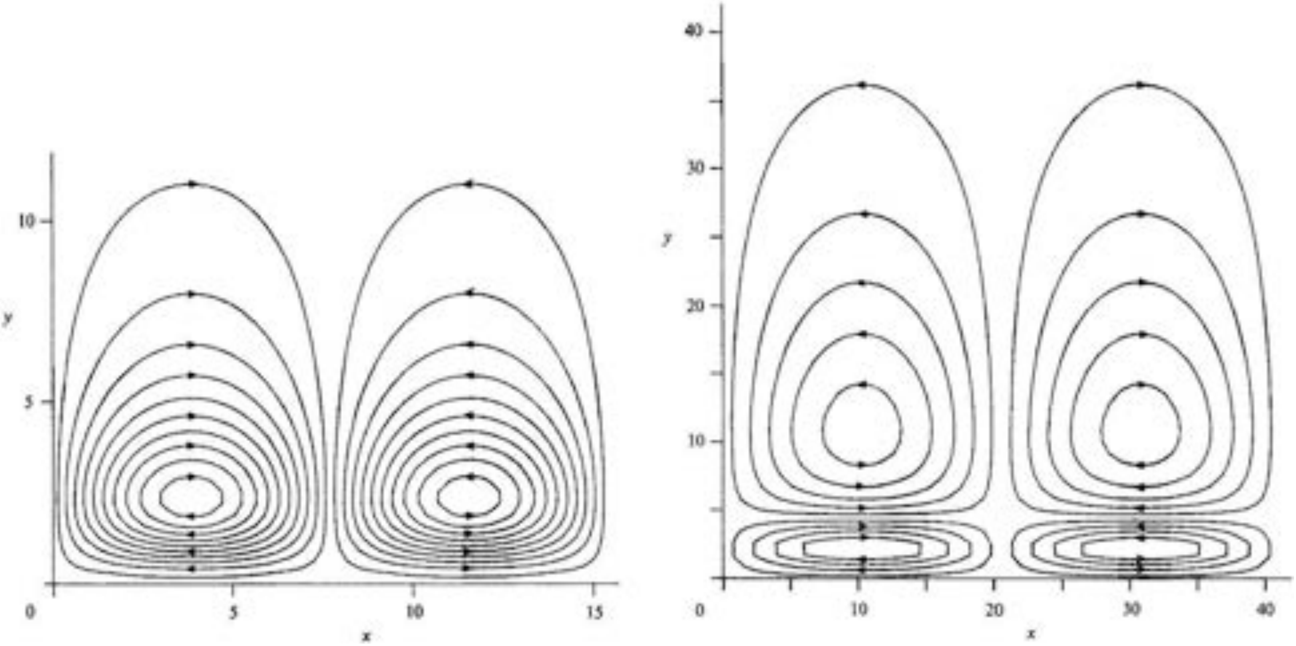

Fig. 8. Streamlines of the steady streaming at order ϵ of the viscous oscillatory flow over a wavy wall plotted in the plane (x, y) (right panel: $\alpha = 0.4, R_\delta = 0.1$; left panel: $\alpha = 0.15, R_\delta = 0.1$) (data from Blondeaux (1990)).

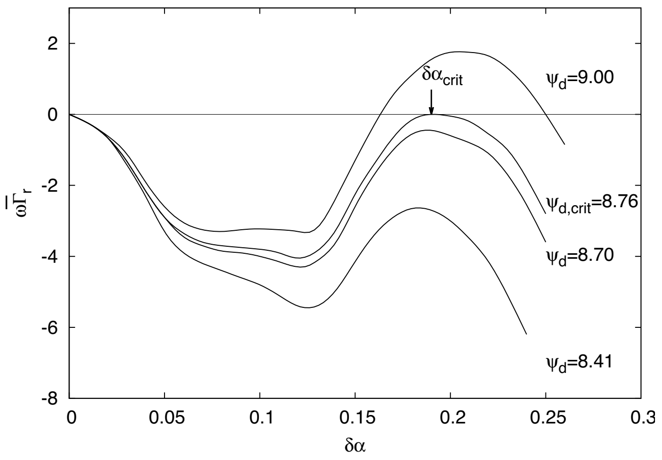

Fig. 9. Growth rate $\overline{\Gamma}_r$ as function of α for $R_\delta = 80, R_d = 80, s = 2.65, \mu_\beta = 0.15, n = 0.4$, n being the porosity of the bottom.

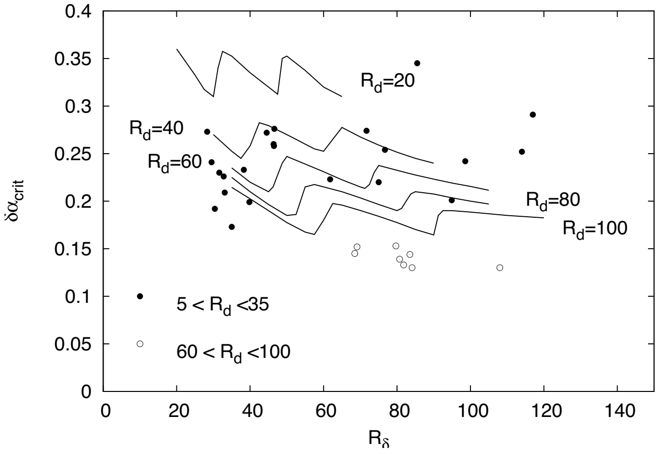

Fig. 10. Critical value α_{crit} of α plotted versus the flow Reynolds number R_δ for $s = 2.65, \mu_\beta = 0.15, n = 0.4$ and different values of R_d.

experimental measurements shows that the analysis provides fair predictions even though it underpredicts the observed wavelengths. The large variations of α_{crit} as function of R_δ for a fixed value of R_d (see Fig. 10) might be caused by changes of the ratio r_r between the amplitude of the sediment displacement oscillations and the ripple wavelength λ_r. During a wave period, a sediment particle is subject to the action of a different number of steady recirculating cells depending on the ratio $\frac{(U_0/\omega)}{\lambda_r}$ between the amplitude of the fluid displacement oscillations and the ripple wavelength.

A further comparison between experimental observations and theoretical values is shown in Fig. 11, where the experimental and theoretical values of the ratio between the amplitude of fluid oscillations and the wavelength of ripples are plotted versus the parameter $\frac{\rho d}{(\rho_s - \rho) g T^2}$, which was suggested by Sleath, 1984 to control the ripple wavelength.

The regions of existence of ripples and flat beds, as predicted by the stability analysis, are shown in Fig. 12 along with the experimental observations of Blondeaux et al. (1988) for a particular set of values of the parameters. Notwithstanding the quantitative differences between the theoretical results and the experimental data mainly due to the inaccuracy of the sediment transport predictor, the stability analysis appears to provide a fair description of the process which leads to ripple formation.

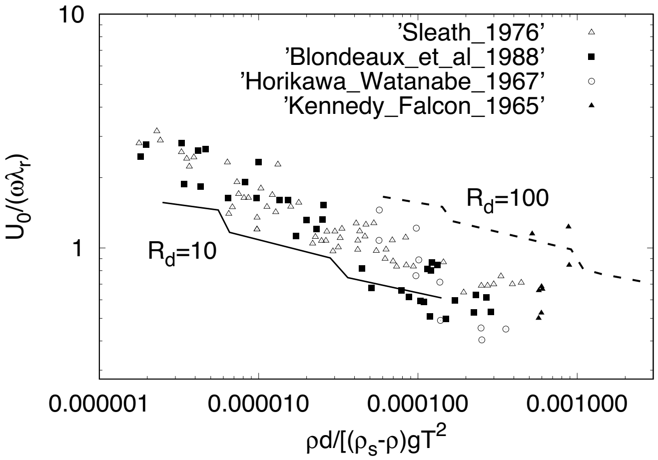

Fig. 11. Ratio between the amplitude U_0/ω of the fluid displacement oscillations and the predicted critical ripple wavelength λ_r plotted versus the parameter $\rho d/(\rho_s - \rho) g T^2$. The experimental values are from different authors (adapted from Blondeaux (1990)).

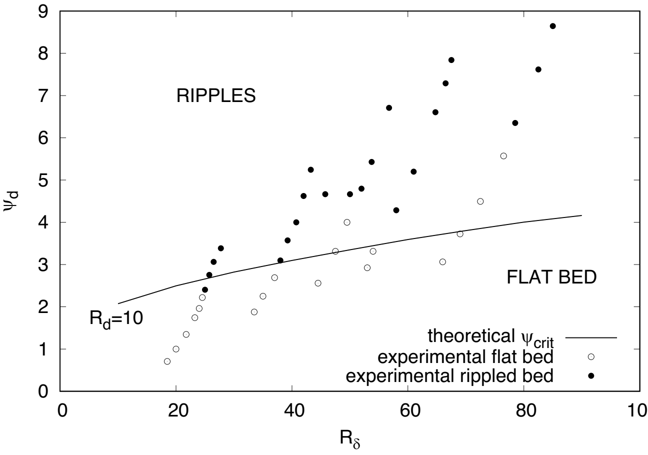

Fig. 12. Regions of existence of ripples and flat beds in the (ψ_d, R_δ)-plane. Experimental observations for $s = 2.65, \mu_\beta = 0.15, n = 0.4$ and $5 < R_d < 15$ (adapted from Blondeaux (1990)).

4.2. *The appearance of vortex ripples for moderate values of R_δ*

The approach of Blondeaux (1990) considers a bottom waviness of small amplitude and neglects nonlinear effects. Hence, it cannot follow the time development of the bottom forms for long times and it cannot determine their equilibrium amplitude. This last information is quite important, since it is known that, for large amplitudes of the bottom forms, the flow separates from their crests and vortices are generated that increase energy dissipation and sediment transport. An attempt to determine the temporal growth of the ripples for long times and to predict the equilibrium amplitude of the bottom forms was made by Vittori and Blondeaux (1990), who extended the analysis of Blondeaux (1990) taking into account weak nonlinear effects. To consider weak nonlinear effects, the value of the sediment Froude number is assumed to be close to the critical value above which ripples form, i.e.

$$F_d = F_{d,crit} + \epsilon F_{d1} \tag{14}$$

and the perturbation is considered to be such that its wavenumber α is provided by

$$\alpha = \alpha_{crit} + \epsilon \alpha_1 \qquad \text{with} \qquad \epsilon \ll 1 \tag{15}$$

In other words, only unstable components with wavelengths slightly different from the critical value are considered.

To be rigorous, it would appear necessary to consider the time development of a narrow spectrum of unstable modes around the critical wavenumber α_{crit}. This would imply to consider the time development of a mode characterized by a wavenumber α_{crit} and an amplitude A which depends not only on a slow temporal scale proportional to $\epsilon\omega t$, as described in the following, but also on the slow spatial scale $\epsilon^{1/2}x/\delta$. Such an analysis leads to a Ginzburg-Landau equation for the amplitude A. However, because of the symmetry of the problem, $\overline{\Gamma}_i$, i.e. the migration speed of the bottom forms, as well as their group velocity vanish. Hence, the coefficients of the Ginzburg-Landau equation would be real. Therefore, close to the critical conditions, the time development of any initial perturbation leads to the appearance of a so-called Stokes wave, i.e. a monochromatic bottom profile characterized by a wavenumber close to α_{crit} (see, a.o. Schielen (1995)).

To solve the problem, Vittori and Blondeaux (1990) used a multiple scale approach (Nayfeh (2011)) and introduced a slow time scale $\tau = \epsilon Q\omega t$ that describes the growth of the ripples. The time variable τ turns out to be much slower then t for two reasons. First, the morphodynamics changes take place on a slow time scale because the parameter Q, which is defined in Vittori and Blondeaux (1990) and depends on the characteristics of the sediment grains, turns out to be much smaller than one. Then, as it happens in all the weakly nonlinear stability analyses, $\tau \propto \epsilon t$ because of (14). Indeed, because of the assumptions (14) and (15), the growth rate of the bottom perturbation is expected to be of order ϵ. Using a multiple scale approach, the time derivatives can be transformed according to

$$\frac{\partial}{\partial t} \rightarrow \frac{\partial}{\partial t} + \epsilon Q\omega \frac{\partial}{\partial \tau}$$

Then, it is necessary to obtain the unknown order of magnitude of both the bottom perturbation and the stream-function. The nonlinearity of the momentum equation gives rise to the interaction of the fundamental component of the bottom perturbation with the basic flow and to its self-interaction. As in the linear analysis, the former interaction makes the perturbed flow to have all the temporal harmonics components. By analysing in details the interaction process, it can be verified that the fundamental spatial harmonic component is reproduced at the third order of approximation and it would generate secular terms which produce a secular growth. The generation of secular terms can be supressed, only by the slow time dependence of the amplitude of the fundamental component that produces a contribution to the third order of approximation. This implies that the amplitude of the bottom perturbation be of order $\epsilon^{1/2}$. The arguments above suggest that the stream function should be expanded in the form

$$\begin{aligned} \psi = {} & \psi_0 + \epsilon^{\frac{1}{2}}\left[A(\tau)C_1(t)\psi_1(y,t)e^{i\alpha x} + c.c.\right] + \epsilon\left[A(\tau)A^*(\tau)C_1(t)C_1^*(t)\psi_{20}(y,t)\right. \\ & \left. + A^2(\tau)\left(C_1^2(t)\psi_{22}^{(1)}\left(y,t\right) + C_{22}(t)\psi_{22}^{(2)}\left(y,t\right)\right)e^{2i\alpha x} + c.c.\right] \\ & + \epsilon^{\frac{3}{2}}\left[A^2(\tau)A^*(\tau)\left(C_1^2(t)C_1^*(t)\psi_{31}^{(1)}\left(y,t\right) + C_{31}(t)\psi_{31}^{(2)}\left(y,t\right)\right)e^{i\alpha x} + c.c.\right] \\ & + O\left(\epsilon^{\frac{3}{2}}e^{3i\alpha}\right) \end{aligned} \tag{16}$$

and the bottom profile turns out to be

$$\begin{aligned} \eta = {} & \epsilon^{\frac{1}{2}}\left[A(\tau)C_1(t)e^{i\alpha x} + c.c.\right] + \epsilon\left[A^2(\tau)C_{22}(t)e^{2i\alpha x} + c.c.\right] \\ & + \epsilon^{\frac{3}{2}}\left[A^2(\tau)A^*(\tau)C_{31}(t)e^{i\alpha x} + c.c.\right] + O\left(\epsilon^{\frac{3}{2}}e^{3i\alpha}\right) \end{aligned} \tag{17}$$

where $A(\tau)$ describes the time development of the amplitude of the bottom perturbation (averaged over the wave cycle), whereas C_i and C_{ij} describe the small periodic changes of the bottom profile taking place during the wave cycle. Moreover, A^*, C_1^* denote the complex conjugates of A and C_1, respectively. As pointed out by Vittori and Blondeaux (1990), different contributions can be recognized in (16). The first term ψ_0 of the expansion (16) describes the basic Stokes flow within the bottom boundary layer over a flat bottom. The term of order $\epsilon^{\frac{1}{2}}$ describes the flow due to the interaction of the oscillatory basic flow with the wavy bottom profile. At order ϵ there are three terms. The first two terms, which are proportional to C_1^2 and $C_1C_1^*$, originate because of the nonlinearity of momentum equation. The third term is due to a bottom waviness characterized by an amplitude ϵC_{22} and a wavenumber 2α. At order $\epsilon^{\frac{3}{2}}$, the term that we are interested in is the term proportional to $C_1^2C_1^*e^{i\alpha x}$, since it reproduces the spatial periodicity of the original perturbation and might cause the secular growth of the perturbation.

The problems which provide ψ_{ij} are long and tedious to be obtained but their derivation is straightforward. The solutions of these problems can be found with a procedure which assumes $\psi = \sum_{m=-\infty}^{\infty} G_{ij}^{(m)}(\widetilde{y})e^{im\omega t}$. Systems of coupled ordinary differential equations for $G_{ij}^{(m)}(\widetilde{y})$ are obtained, which can be solved by means of a standard Runge-Kutta method of forth-order and a shooting procedure (Vittori (1989)). Once the stream functions at the different order of approximation are determined, sediment continuity equation provides the values of $C_{ij}(t)$.

Sediment continuity equation at order $\epsilon^{\frac{1}{2}}$ suggests that C_1 is a periodic function of t of $O(Q)$. Considering the terms of $O(\epsilon)$ of sediment continuity equation, in order to avoid the secular growth of the perturbation, it is necessary to force a condition that provides the amplitude C_{22} of the second harmonic of the bottom waviness and shows that the profile of the ripples is characterized by crests that are sharper than the troughs. Similarly, considering the terms of sediment continuity equation of $O\left(\epsilon^{\frac{3}{2}}\right)$, to avoid the secular growth of the perturbation, it is necessary to force the following amplitude equation

$$\frac{dA(\tau)}{d\tau} = a_1A(\tau) + a_2A^2(\tau)A^*(\tau) \tag{18}$$

where a_1 and a_2 are coefficients that depend on the hydrodynamic and morphodynamic parameters. The amplitude Eq. (18) is of Landau-Stuart type and it can be integrated to obtain the time development of the amplitude of the bottom perturbation

$$|A(\tau)| \;\; = \sqrt{\frac{\mathrm{Real}(a_1)}{exp[-2\mathrm{Real}(a_1)\tau] - \mathrm{Real}(a_2)}} \tag{19}$$

If nonlinear effects are neglected (i.e. a_2 is set equal to zero), the exponential growth/decay of the bottom perturbation, obtained by means of the linear stability analysis, is recovered.

When a_1 is positive and $|A|^3$ is not negligible with respect to $|A|$, nonlinear effects modify the exponential growth of the perturbation and the amplitude might attain the finite equilibrium value $|A_e|$

$$|A_e| \;\; = \sqrt{-\frac{\mathrm{Real}(a_1)}{\mathrm{Real}(a_2)}} \tag{20}$$

Of course $\mathrm{Real}(a_2)$ should be negative. If the values of the parameters are such that $\mathrm{Real}(a_2)$ is positive, no equilibrium exists and the perturbation grows till nonlinear effects become so strong that the weakly nonlinear approach fails. In this case vortex ripples are expected to appear and the strong nonlinear effects generated by the boundary layer separation allow an equilibrium to be attained.

Vittori and Blondeaux (1990) showed that the plane (R_δ, ψ_d) can be divided into three regions, the boundaries of which depend on the values of the parameters. A first region is identified by values of ψ_d smaller than $\psi_{d,crit}$. In such a region the flat bottom is stable and ripples are not expected to appear. On the other hand, for ψ_d larger than $\psi_{d,crit}$, the analysis predicts the formation of ripples. In the sub-region such that $\mathrm{Real}(a_2)$ is negative and the ratio between the predicted height of the ripples and the predicted length turns out to be smaller than about 0.1, which is the limiting value for flow separation at the ripple crests (Sleath

(1984)), the analysis predicts the appearance of rolling grain ripples as equilibrium bedforms. In the sub-region such that Real(a_2) is negative but the ratio between the predicted height of the ripples and the predicted wavelength turns out to be larger than about 0.1 or in the sub-region such that Real(a_2) is positive, the weakly nonlinear analysis shows that no equilibrium is possible assuming that nonlinear effects are weak. In this case the amplitude of the bottom forms tends to grow till the boundary layer separates from the ripple crests and vortex ripples are generated.

A comparison between the theoretical predictions and the experimental observations of Blondeaux et al. (1988) and Horikawa and Watanabe (1968) is shown in Figs. 13 and 14, respectively. If rolling grain ripples are the equilibrium bottom forms predicted by the weakly nonlinear stability analysis, it is also possible to predict the amplitude of the ripples. Fig. 15 shows a comparison between the predicted values of the ratio between ripple height and δ and the values measured by Blondeaux et al. (1988). The qualitative agreement is satisfactory taking into account that the empirical formulae, which can be found in the literature to predict the sediment transport rate, often provide its order of magnitude but not an accurate quantitative value (see a.o. fig. 2.3.2 of Nielsen (1992)).

At this stage, it is worth pointing out that the presence of isolated disturbances of large amplitude can modify the mechanism of ripple appearance previously described. The growth of ripples from isolated disturbances of the bottom has not been investigated by means of stability analyses so far. The study of a possible mechanism leading to the formation of periodic bedforms from an isolated disturbance was carried out by Roos et al. (2005) by considering the large scale bedforms (sand waves) generated by tidal currents. The mechanism outlined by Roos et al. (2005), even though acting on a different spatial scale, provides a possible explanation of the morphological patterns shown by Figs. 16 and 17 that were observed by Taylor Perron and Jaap Nienhuis (2018, private communication) during a laboratory experiment made in a wave channel. In the experiments, surface waves propagating over a water depth of 40 cm and characterized by a period of 2.6 s and a height of 6.4 cm modelled the bottom of the wave flume and caused the appearance of ripples that started at a particular location and then spread all over the flume bottom. A further investigation of ripples appearance triggered by an isolated disturbance was made by Sekiguchi and Sunamura (2004), who investigated the appearance of ripples by considering an initial flat bed with and without a localized large amplitude perturbation and observed that, when the mobility number ψ_d is larger that 2.5, ripples start from the localized perturbation and pervade the whole sediment bed.

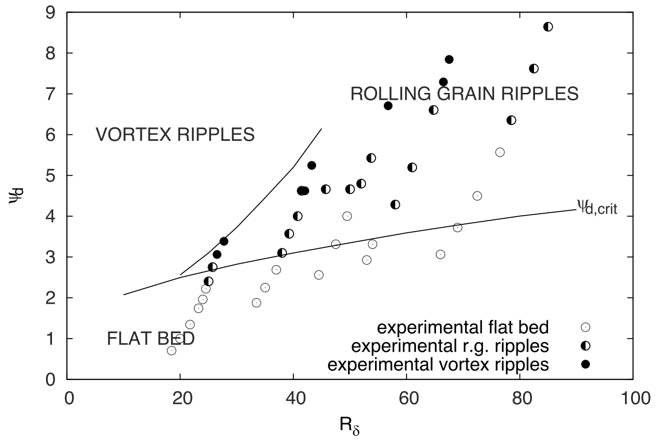

Fig. 13. Regions in the (R_δ, ψ_d)-plane where a flat bed, rolling-grain ripples (r. g. ripples), vortex ripples are expected to appear. Comparison between the theoretical predictions $(R_d = 10, s = 2.65)$ and the laboratory observations $(5 < R_d < 10)$ of Blondeaux et al. (1988).

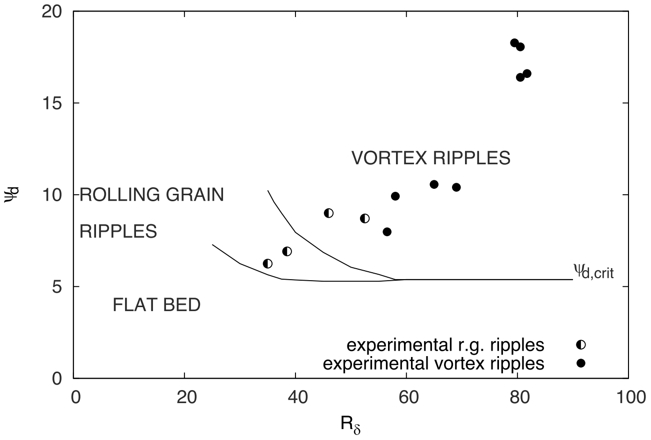

Fig. 14. Regions in the (R_δ, ψ_d)-plane where a flat bed, rolling-grain ripples (r. g. ripples), vortex ripples are expected to appear. Comparison between the theoretical predictions $(R_d = 40, s = 2.65)$ and the laboratory observations $(30 < R_d < 50)$ of Horikawa and Watanabe (1968).

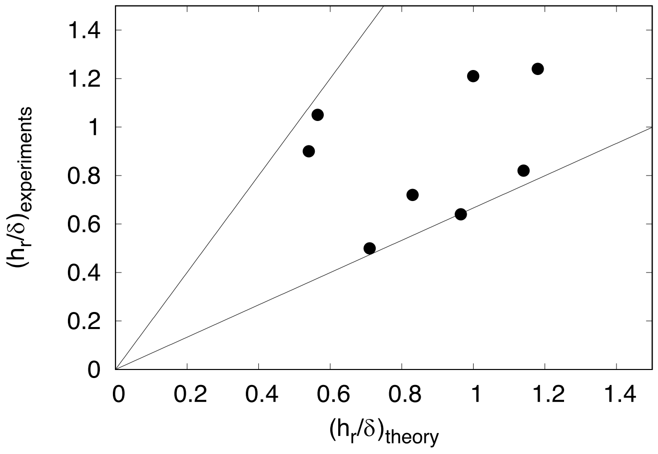

Fig. 15. Comparison between theoretical and experimental values of the height h_r of rolling-grain ripples (experimental data of Blondeaux et al. (1988)). The two straight lines indicate an error of the theoretical predictions equal to 50%.

4.3. The appearance of brick-pattern and tile ripples for moderate values of R_δ

Even though the ripple profile is often two-dimensional, other ripple shapes are observed depending on sediment and flow characteristics. For example, Fig. 18 shows a photo of the brick-pattern ripples observed by Sleath (1984) during a laboratory experiment. The main crests of the brick pattern ripples are perpendicular to the direction of the fluid oscillations, as for two-dimensional ripples, but these crests are joined by equally spaced sand bridges of small amplitude which are parallel to the direction of the fluid oscillations and shifted, between adjacent sequences, in the transverse direction by half the transverse wavelength. Hence, the bottom topography resembles a wall of bricks. Other three-dimensional ripples do exist and photos can be found in the books of Sleath (1984) and Allen (1982) (see also Fig. 19).

A possible mechanism able to trigger the formation of brick-pattern ripples was first described by Hara and Mei (1990a) and Hara and Mei (1990b), who considered the stability of the Stokes boundary layer over a wavy wall and investigated the time development of spanwise perturbations of this two-dimensional basic flow field. Hara and Mei (1990a, 1990b) showed that the growth of the flow perturbations might lead to a three-dimensional flow which is periodic with either a wavelength equal to that of the two-dimensional bottom waviness or a

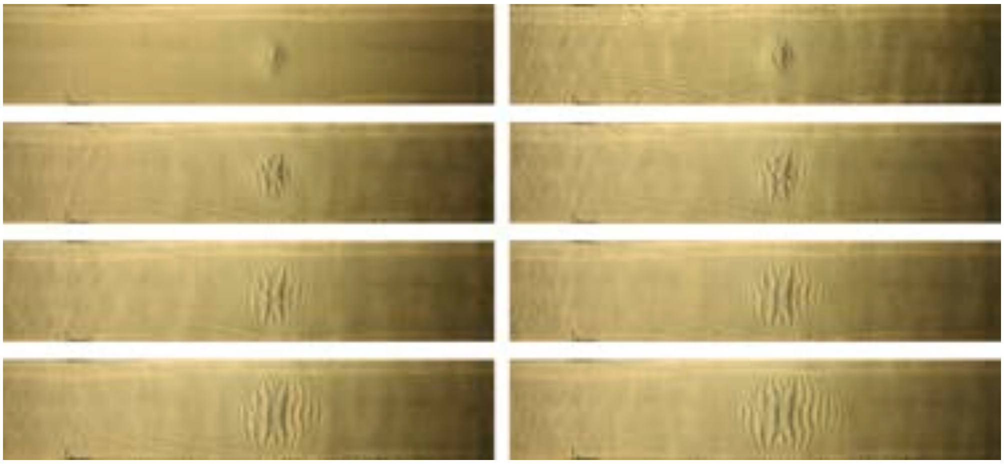

Fig. 16. The time development of an isolated bottom bump subject to a propagating wave which leads to the appearance of a rippled bed. The first panel (the panel on the top-left of the figure) shows the initial bottom configuration and the other panels show bottom configurations which are 260 s apart (plotted counter-clockwise) (courtesy of Taylor Perron). The characteristics of the surface wave are give in the text.

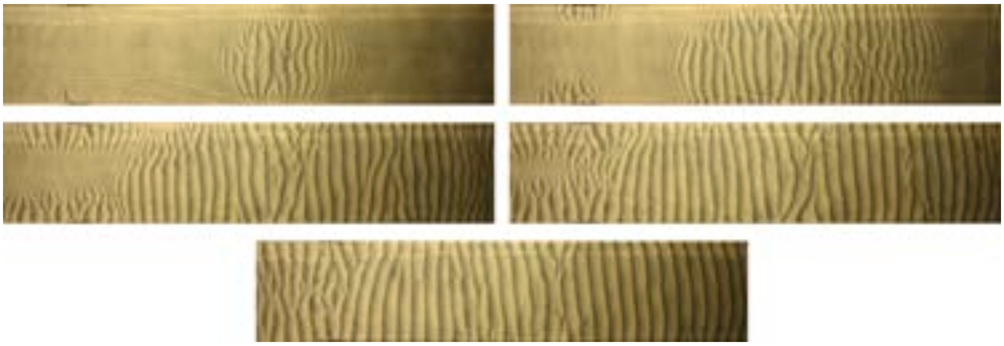

Fig. 17. The time development of an isolated bottom bump subject to a propagating wave which leads to the appearance of a rippled bed. The first panel shows the bottom configuration at 2600 s from the beginning of the experiment and the other panels are 2600 s apart (courtesy of Taylor Perron). The characteristics of the surface wave are give in the text.

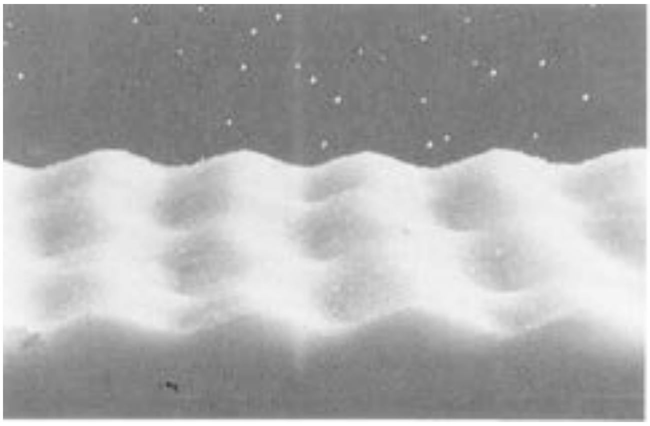

Fig. 18. Brick-pattern ripples observed during a laboratory experiment (courtesy of John F.A. Sleath).

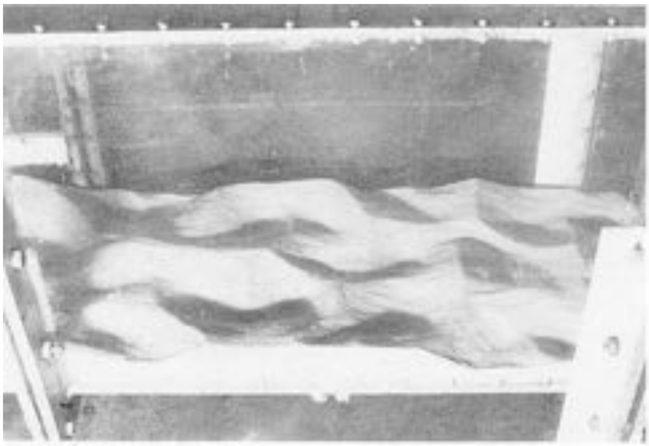

Fig. 19. Three-dimensional vortex ripples observed during a laboratory experiment (courtesy of John F.A. Sleath).

wavelength which is twice the previous one, depending on the values of the parameters. Hence, the steady velocity component, which is originated by the growth of the perturbation, tends to accumulate the sand in various patterns. One of these patterns suggests the initiation of brick-pattern ripples. Later Vittori and Blondeaux (1992) explained the formation of brick-pattern ripples by developing a weakly nonlinear stability analysis of a sandy bottom subject to an oscillatory flow. The analysis of Vittori and Blondeaux (1992) considers three-dimensional perturbations of the bottom profile and shows that brick-pattern ripples can be originated by the simultaneous growth of two-dimensional and three-dimensional perturbations of the sea bottom that interact with a mechanism similar to that described by Craik (1971) in a different context. The analysis of Vittori and Blondeaux (1992) considers the

Stokes boundary layer over a flat bottom as basic flow. Then, Vittori and Blondeaux (1992) argued that the critical value of the mobility number for the growth of two-dimensional perturbations $(F_d)_{c2}$ is close to that which leads to the instability of three-dimensional perturbations $(F_d)_{c3}$. Then, Vittori and Blondeaux (1990) assumed

$$F_d = (F_d)_{c2} + \epsilon k_2 = (F_d)_{c3} + \epsilon k_3 \tag{21}$$

and considered the following three components of a bottom perturbation, which are shown to strongly interact

$$y = \epsilon\left[A_1(\tau)C_1(t)e^{i\beta x} + A_2(\tau)C_2(t)e^{i(\alpha x+\gamma z)} + A_3(\tau)C_3(t)e^{i(\alpha x-\gamma z)} + c.c.\right] + O\left(\epsilon^2\right) \tag{22}$$

The reader should be aware that (21) implies that the mobility number ψ_d is close to its critical values $(\psi_d)_{c2}$ and $(\psi_d)_{c3}$ since (21) can be written as $\sqrt{\psi_d} = \sqrt{(\psi_d)_{c2}} + \epsilon k_2 = \sqrt{(\psi_d)_{c3}} + \epsilon k_3$. Since the values of the parameters are close to the critical ones, the amplitude of the perturbations grows on the slow time scale τ that is proportional to ϵ because of (21). On the other hand $C_1(t), C_2(t), C_3(t)$ describe the periodic oscillations of the bottom profile which take place during the wave cycle. The flow field, as well as the other variables, are expanded in a similar way as (22). Because of (21), the functions A_i neither grow nor decay because the value of the sediment Froude number at this order of approximation concides with the critical value for the growth of the bottom perturbations. Hence, the functions C_i keep constant but for small periodic oscillations of the bottom profile during the wave cycle, which are of order ϵQ and have a vanishing average.

The analysis of Vittori and Blondeaux (1992) shows that at $O\left(\epsilon^2\right)$, if $\beta = \alpha/2$, the interaction of the three components of the bottom perturbation would induce a secular growth of their amplitudes, unless the following solvability conditions are forced

$$\frac{dA_1}{d\tau} = a_1A_1 + b_1A_2A_3; \quad \frac{dA_2}{d\tau} = a_2A_2 + b_2A_1A_3^*; \quad \frac{dA_3}{d\tau} = a_3A_3 + b_3A_1A_2^* \tag{23}$$

where a_i, b_i are real constants that depend on the parameters of the problem. Moreover, the symmetries of the problem force $a_2 = a_3$, $b_2 = b_3$ and suggest to assume $A_2 = -A_3$.

The behaviour of A_i depends, beside the parameters of the problem, on the initial values $A_i(0)$, which in the following are assumed to be small. The values of a_i depend on how far the actual values of the parameters are from the critical values. Moreover, for assigned values of the parameters, b_i depend on γ, i.e. the wavenumber of the perturbation in the spanwise direction.

To illustrate the results of the analysis, let us follow Vittori and Blondeaux (1992) and consider values of F_d larger than the critical value $(F_d)_{c2}$ of the sediment Froude number for the growth of two-dimensional disturbances but smaller than the critical value $(F_d)_{c3}$ that leads to the growth of three-dimensional disturbances that is assumed to be larger than the former. In this case, the linear analysis would predict the growth of two-dimensional ripples only. However, the numerical integration of (23) shows that two different behaviour of A_i can be observed depending on the values of the other parameters. In some cases (see Fig. 20), only A_1 grows while A_2 and A_3 decay and thus the analysis predicts the appearance of two-dimensional ripples. In these cases nonlinear effects are too weak to modify the time development of the sea bed predicted by the linear stability analysis. However, values of the parameters do exist such that all the three components of the bottom perturbation grow (see Fig. 21) and a bottom configuration similar to that of brick-pattern ripples tends to appear (see Fig. 21).

Figs. 20 and 21 show the behaviour of A_i for values of the parameters chosen to reproduce the experiments number 76 and 49 of Sleath and Ellis (1978). In the former case only the two-dimensional component of the perturbation grows whereas in the latter case also the three-dimensional components grow. In other words the weakly nonlinear stability analysis, accordingly with Sleath and Ellis (1978) observations, predicts the appearance of two-dimensional ripples during experiment number 76 and three-dimensional ripples similar to brick pattern ripples during experiment number 49.

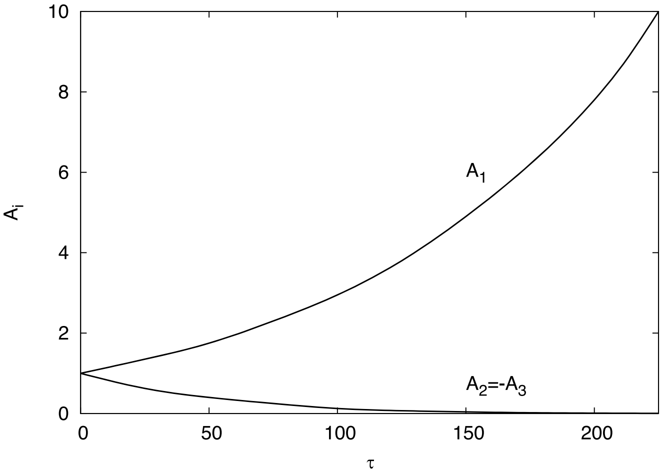

Fig. 20. Time development of the amplitude A_i $(i = 1, 2, 3)$ for $R_d = 30, R_\delta = 50, F_d = 2.15, \gamma = 0.14, \epsilon = 0.1$, $(s = 2.65, \mu_\beta = 0.15)$.

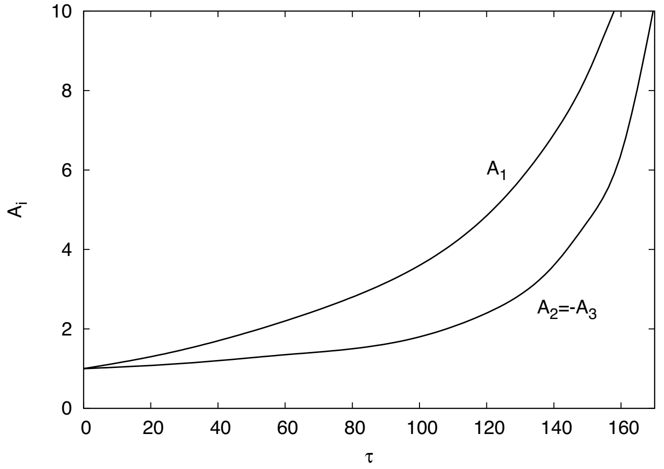

Fig. 21. Time development of the amplitudes $A_i (i = 1, 2, 3)$ for $R_d = 30, R_\delta = 68, F_d = 2.15, \gamma = 0.14, \epsilon = 0.1$, $(s = 2.65, \mu_\beta = 0.15)$.

The numerical integration of (23) for different values of the parameters along with the results obtained by Blondeaux (1990) and Vittori and Blondeaux (1990) shows that the parameter space can be divided into four different regions where the stability analysis predicts (i) a stable flat bed, (ii) the appearance of rolling-grain ripples, (iii) the appearance of vortex ripples, (iv) the appearance of brick-patterns ripples. Fig. 22 shows an example of the results along with the experimental results of Sleath and Ellis (1978) and Horikawa and Watanabe (1968). Of course, when the analysis predicts the appearance of brick-pattern ripples, the trasverse wavelength of the bottom forms can be predicted, too. In Fig. 23, the experimental values of the transverse wavenumber γ measured by Sleath and Ellis (1978) are plotted along with the theoretical predictions.

To conclude this section, let us point out that Mei and Liu (1993) and Blondeaux and Vittori (1999) pointed out that values of the parameters might exist such that the length and time scales characteristic of the flow instability mechanism described by Hara and Mei (1990a) become comparable with those found by analysing the stability of the bottom and the two mechanisms may interact giving rise to a complex bottom

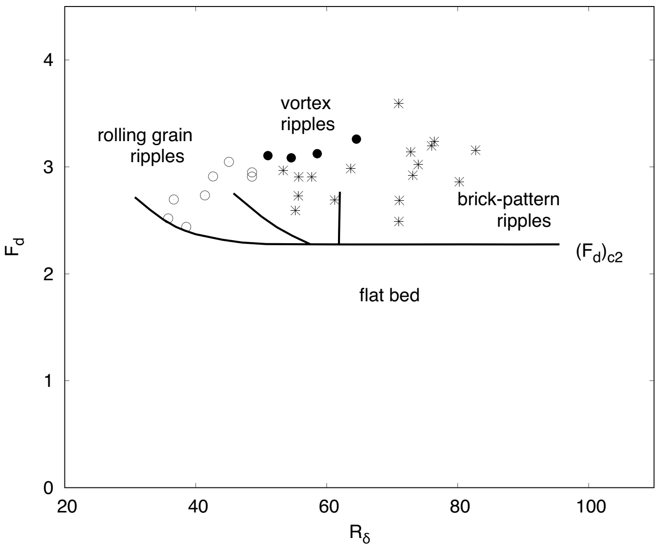

Fig. 22. Limiting curves dividing the (R_δ, F_d)-plane in regions where a flat bed, rolling grain ripples, two-dimensional vortex ripples, brick-pattern ripples are expected to form $(R_d = 40, s = 2.65, \mu_\beta = 0.15)$. Also shown are the experimental data by Sleath and Ellis (1978) and Horikawa and Watanabe (1968) for $35 < R_\delta < 45$ (white points = rolling grain ripples, black points = vortex ripples, stars = brick pattern ripples). Adapted from Vittori and Blondeaux (1992).

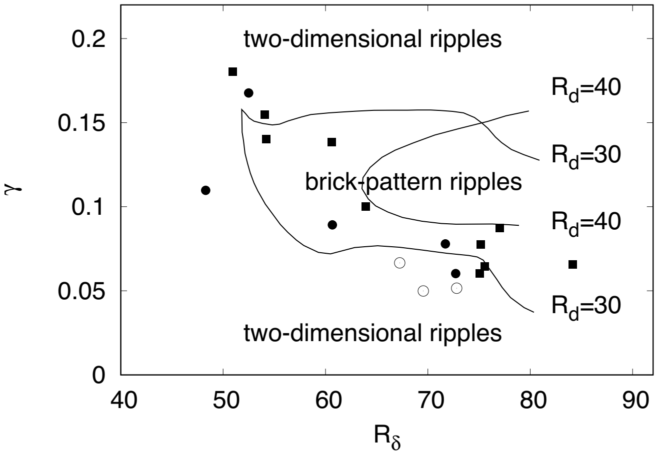

Fig. 23. Range of γ within which the brick pattern ripples can appear, plotted versus R_δ for $R_d = 30$ and 40 $(s = 2.65, \mu_\beta = 0.15)$. Experimental data of the transverse wavenumber by Sleath and Ellis (1978) are for $30 < R_d < 40$. Adapted from Vittori and Blondeaux (1992).

morphology.

Roos and Blondeaux (2001) performed a study similar to that of Vittori and Blondeaux (1992) but considered a forcing flow generated by the simultaneous presence of two surface waves characterized by the same angular frequency but different amplitudes and directions of propagation. Such a wavefield can be observed when a wave is partially reflected by a coastal structure. In this case, close to the bottom, the irrotational flow is not unidirectional but characterized by an elliptical behaviour. The results by Roos and Blondeaux (2001) indicate the possible formation of hexagonal ripples, also named tile ripples. A photo of such ripples can be found in Allen (1982).

4.4. *The appearance of ripples for large values of R_δ*

The analyses previously summarized explain the appearance of ripples and predict their geometrical characteristics at incipient formation but only for moderate values of the Reynolds number, such that the flow regime in the boundary layer at the bottom of sea waves is laminar. However, under field conditions, the Reynolds number R_δ is often large and turbulence appears (Mazzuoli et al. (2011); Mazzuoli and Vittori (2019); Mazzuoli et al. (2018); Vittori et al. (2020a)). The linear stability analysis by Blondeaux (1990) was extended to consider the turbulent regime by Foti and Blondeaux (1995a), who considered the Reynolds averaged momentum equations and used a simple turbulence model. In particular, Foti and Blondeaux (1995a) modelled the Reynolds stresses by introducing a turbulent kinematic eddy viscosity ν_T that has a constant value in time and is independent of the distance from the sea bottom. An acceptable description of the flow within the bottom boundary layer can be obtained by considering a constant value of ν_T, if the no-slip condition at the bottom is replaced by a partial slip condition, as suggested by Engelund and Fredsoe (1982) in another context.

Of course, the details of the flow close to the bed, where the velocity gradient in the vertical direction is very large, are not reproduced by the model. Notwithstanding this deficiency, the approach provides fair estimates of the bed shear stress, because the unrealistic large values assumed by the eddy viscosity close to the bed balance the unrealistic small values of the velocity gradient induced by the partial slip condition. The interested reader is referred to Engelund and Fredsoe (1982) and Sleath (1991) for a detailed discussion of this approximation.

A best fitting procedure suggests that the constant value of the eddy viscosity can be fixed equal to $\nu_T = \frac{0.1}{(2\pi)^2} U_{0r}^{3/2} \sqrt{\frac{k_s}{\omega}}$ where k_s is the Nikuradse roughness, U_{0r} and ω are the amplitude and the angular frequency of the velocity oscillations induced by the surface wave close to the bed, respectively. Because of the presence of the wall waviness, it is necessary to take into account that U_{0r} and the eddy viscosity depend on x. Moreover, the slip velocity proposed by Sleath (1984) is $u_{slip} = -\frac{U_{0r}}{2} \hat{u} e^{i(\omega t - \phi)} + c.c.$ where $\hat{u}$ and ϕ are dimensionless quantities.

The main steps of the analysis of Foti and Blondeaux (1995a) are similar to those of the analysis carried out by Blondeaux (1990). Only vorticity equation is different because of the dependence of ν_T on the streamwise coordinate x. The results are qualitatively similar to those obtained in the laminar case but the extension of the analysis to the turbulent case allows to extend the range of the parameters which can be considered. Fig. 24 shows the wavelength λ_r of the ripples predicted for the turbulent case, i.e. for values of the parameter $\frac{\rho d}{(\rho_s - \rho) g T^2} = \frac{\psi_d^2 R_d^2}{\pi^2 R_\delta^4}$ smaller than those considered by Vittori and Blondeaux (1990) and more relevant for field cases.

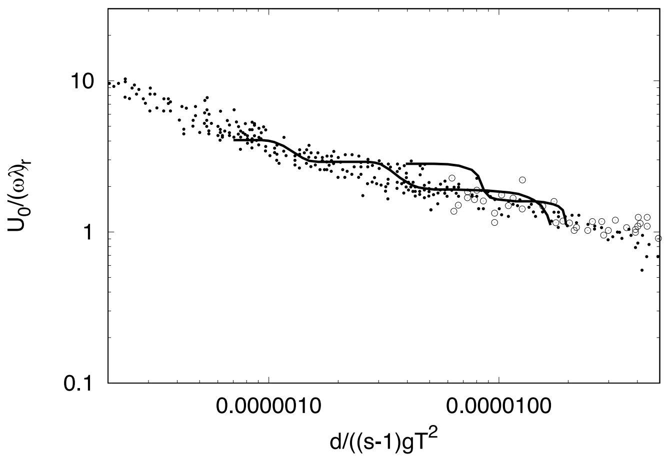

Fig. 24. Ratio between the amplitude U_0/ω of the fluid displacement oscillations and the ripple wavelength λ_r plotted versus the parameter $\rho d/(\rho_s - \rho) g T^2$. The theoretical curves are the result of the stability analysis of Foti and Blondeaux (1995a) while the experimental measurements are those of Manohar (1955) and Sleath (1976) (adapted from Foti and Blondeaux (1995a)).

4.5. Large amplitude ripples and fully nonlinear models

4.5.1. Oscillatory flow over vortex ripples for moderate values of R_δ

Even though the linear and weakly nonlinear stability analyses previously summarized are able to describe the process which gives rise to two-dimensional and three-dimensional ripples and to predict some of their geometrical characteristics, they are no longer valid when the parameters of the problem are far from the critical conditions and the amplitude of the bedforms is no longer small. In this case, nonlinear effects are strong and a perturbation approach can not be used to describe the dynamics of ripples and to predict their time development. Under these circumstances, only the numerical integration of momentum equations along with fluid and sediment continuity equations can be used to determine the flow field and the time development of the bottom forms.

Early attempts to determine the dynamics of the vortices shed by the ripple crests were performed by Longuet-Higgins (1981) and Smith and Stansby (1985), who employed discrete vortex methods. These approaches assume that the free shear layer generated by the boundary layer separation can be modelled as a large number of point vortices that are convected by the flow, which is computed by means of an inviscid approach. Later, the full two-dimensional problem was solved by Shum (1988) and Blondeaux and Vittori (1991a). In particular, Blondeaux and Vittori (1991a) considered a bottom profile described in parametric form by

$$z=\frac{h_r}{2}cos(\alpha\xi), \qquad x=\xi-\frac{h_r}{2}sin(\alpha\xi) \tag{24}$$

where ξ is a dummy variable ranging from $-\infty$ to ∞, α is the wavenumber of the periodic bottom profile and h_r denotes its height (vertical distance between the crests and the troughs of the ripples). As observed in the field, the crests of the bottom forms turn out to be sharper than the troughs. Moreover, a comparison of the profile (24) with experimental data shows a fair agreement (see Sleath (1984), page 70).

To determine the flow field, an orthogonal curvilinear coordinate system (ζ,η) is introduced

$$\zeta=x+\frac{h_r}{2}e^{-\alpha\eta}sin(\alpha\zeta), \qquad \eta=z-\frac{h_r}{2}e^{-\alpha\eta}cos(\alpha\zeta) \tag{25}$$

such that the bottom profile is mapped into the line $\eta=0$. Then, since the flow is assumed to be two-dimensional, the stream function ψ and the vorticity Ω are introduced ($\psi-\Omega$ formulation). A finite difference approach is used to determine the time development of the vorticity field Ω from the vorticity equation and to obtain the stream-function ψ from the Poisson equation which follows from the vortocity definition

$$\frac{\partial^2\psi}{\partial\zeta^2}+\frac{\partial^2\psi}{\partial\eta^2}=-J\Omega \tag{26}$$

where J is the Jacobian of the transformation (25). More details can be found in Blondeaux and Vittori (1991a).

The numerical approach was validated by comparing the results it provides with those of Blondeaux (1990) and Hara and Mei (1990a). Hara and Mei (1990a) determined the oscillatory flow over ripples of large amplitudes, for small values of the ratio between the amplitude of the fluid oscillations and the ripple wavelength. Fig. 25 shows the steady velocity component provided by the numerical solution of Blondeaux and Vittori (1991a) that is almost coincident with the results of Hara and Mei (1990a) which describe only the flow close to the bottom. However, the flow keeps attached to the bottom and flow separation is absent. Fig. 26 shows an example of the results obtained by Blondeaux and Vittori (1991a) for a ripple profile and a value of the Reynolds number which induce flow separation from the ripple crests and the generation of a free shear layer. The flow starts from rest and the horizontal velocity far from the bottom progresses as $U_0 sin(2\pi t/T)$. At the beginning, the free stream is directed from the left to the right and clockwise vorticity is generated along the bed profile and particularly close to the crest of the ripple (Fig. 26a,b). Then, the boundary layer thickens on the downstream side of the bottom forms till flow separates and vorticity of opposite sign is generated (Fig. 26c). The clockwise vorticity rolls up and gives rise to a well defined vortex (Fig. 26c,d). When the free stream velocity reverses, the clockwise vortex is no longer fed and it is simply convected from the right to the left by the local flow (Fig. 26e,f). Meanwhile, counter-clockwise vorticity is shed from the crest and the phenomenon repeats similarly during the following half cycle (Fig. 26g, h). The characteristic of the oscillatory flow over large amplitude ripples is the generation of vortex pairs which move because of the external flow and the self-induced velocity (Saffman (1995)). Of course, the size, the strength and the number of vortex structures generated by the oscillatory flow over a rippled bed depend on the parameters of the problem (Blondeaux and Vittori (1991b)).

When the bottom is made up of cohesionless sediments, the vortices pick up the sediments from the bed and carry them into suspension.

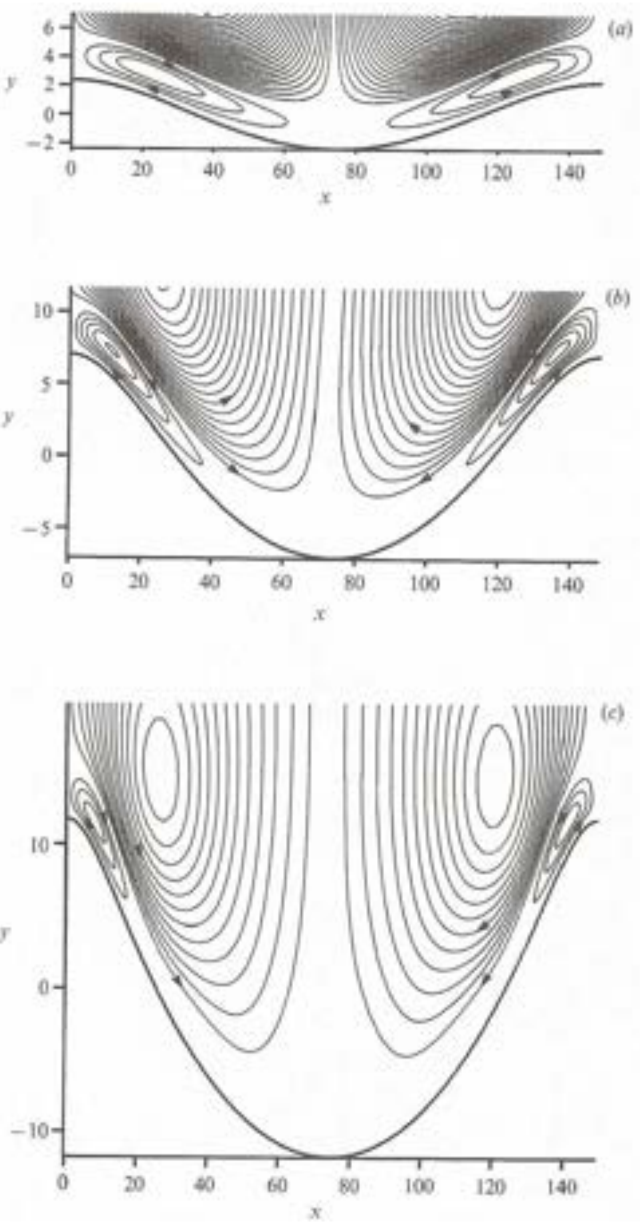

Fig. 25. Contours of the time averaged stream function of the oscillatory flow over a wavy wall for $\frac{2\pi\delta}{\lambda_r}=0.0424, R_\delta=14.14$ (figure from Blondeaux and Vittori (1991a)): a) $h_r/\delta=4.71$, b) $h_r/\delta=14.14$, c) $h_r/\delta=23.57$.

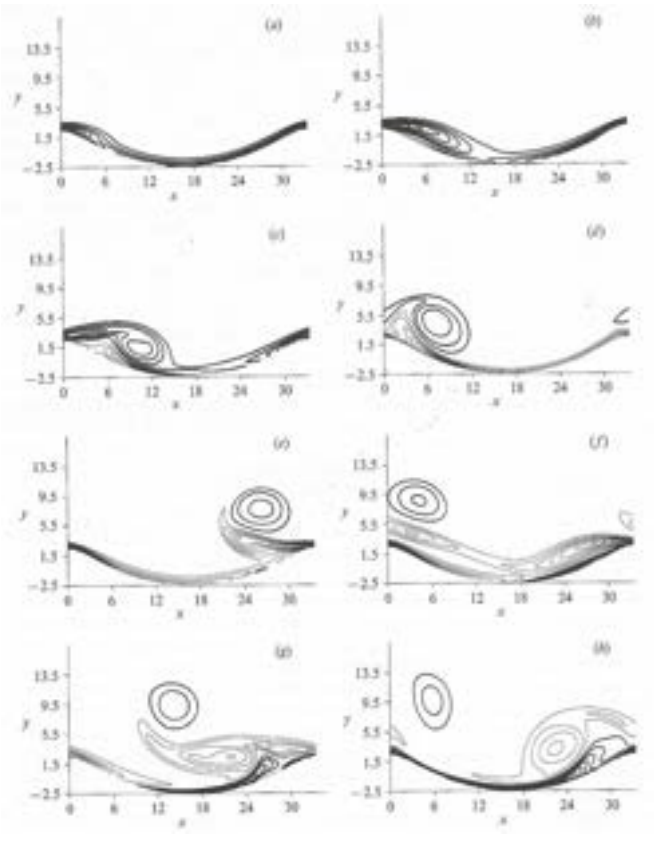

Fig. 26. Vorticity contours of the oscillatory flow over a wavy wall $R_\delta = 50$, $h_r/\lambda_r = 0.15, U_0/(\omega\lambda_r) = 0.75$ ($\Delta\Omega = 0.15\frac{U_0}{\delta}$, thick lines = clockwise vorticity, thin lines = counter-clockwise vorticity). a) $\omega t = \pi/4$; b) $\omega t = \pi/2$; c) $\omega t = 3\pi/4$; d) $\omega t = \pi$; e) $\omega t = 5\pi/4$; f) $\omega t = 3\pi/2$; g) $\omega t = 7\pi/4$; h) $\omega t = 2\pi$ (figure from Blondeaux and Vittori (1991a)).

Attempts to compute the dynamics of sediment particles can be made using a Lagrangian approach. Blondeaux and Vittori (1991b) attempted to model the motion of sediment grains over a rippled bed using the flow field computed by Blondeaux and Vittori (1991a). A significant improvement of the model was achieved by Hansen et al. (1994), who employed a discrete vortex method to determine the time development of the vortex structures generated by the boundary layer separation at ripple crests. The assumption of a two-dimensional flow limits the validity of the approach to moderate values of the Reynolds number. As discussed previously, the stability analysis of Hara and Mei (1990b) shows that the two-dimensional vortex structures generated at the ripple crests might be unstable and give rise to a three-dimensional flow. Hara and Mei (1990b) suggested that the transition from a two-dimensional to a three-dimensional flow is due to the centrifugal three-dimensional instability of the two-dimensional flow over two-dimensional ripples. The physical mechanism which causes the appearance of these disturbances is similar to that leading to the growth of spanwise disturbances of the oscillatory flow around a circular cylinder for amplitudes of the fluid oscillations much smaller than the radius of the cylinder (Hall (1984)).

Later, Blondeaux and Vittori (1999) and Scandura et al. (2000) made direct numerical simulations (DNS) of the three-dimensional oscillatory flow over two-dimensional ripples considering large values of both the ripple steepness and the amplitude of the fluid oscillations. The results of these DNSs extend the analysis of Hara and Mei (1990a) and give further information on the process through which the oscillatory flow over two-dimensional ripples becomes three-dimensional. In particular, Blondeaux and Vittori (1999) and Scandura et al. (2000) showed that the nonlinear terms, which were not considered by Hara and Mei (1990a), have different effects which depend on the values of the parameters.

Scandura et al. (2000) considered also cases characterized by amplitudes of the fluid oscillations of the same order of magnitude as the ripple wavelength and a significant ripple steepness, even though these cases were characterized only by moderate values of the Reynolds number. In these cases, it was shown that the vorticity dynamics tend to generate vortex structures similar to mushroom vortices.

Blondeaux and Vittori (1999) investigated sediment dynamics using the same code of Scandura et al. (2000) to evaluate the flow field and mimicking sediment transport by evaluating the trajectories of the 'passive' sediment particles (one-way copupling). Even though further simulations are required to investigate the phenomenon for larger values of the Reynolds number, it appears that the three-dimensional vortex structures, generated by the spanwise instability of the basic two-dimensional flow, strongly affect particle trajectories and create relevant dispersion effects. When the Reynolds number is further increased, the large scale coherent vortices break down into smaller three-dimensional structures and turbulence appears.

4.5.2. *Oscillatory flow over vortex ripples for large values of R_δ*

Barr et al. (2004) studied the oscillatory flow over a rippled bed for large values of the Reynolds number, by means of a numerical approach that considers and solves momentum (Navier-Stokes) and continuity equations using a curvilinear coordinate system which follows the bottom profile (Winters et al. (2000)). The numerical approach is standard and uses a third-order Adams-Bashforth approach and a fourth-order compact spatial difference scheme to advance in time and to approximate the spatial derivatives, respectively. Moreover, a fourth-order multigrid method is employed to determine the pressure field which is obtained from the Poisson equation (Adams (1991)). Even though the code used by Barr et al. (2004) allows also the use of the LES approach, their paper focuses mainly on the results obtained by means of Direct Numerical Simulations (DNS) of continuity and Navier-Stokes equations, thus avoiding the introduction of a subgrid scale model.

By comparing the oscillatory flow field over a rippled bed with that over a flat bed, Barr et al. (2004) showed that the ripple presence leads to a significant increase of the thickness of the bottom boundary layer because of the vortices shed at the ripple crests and the consequent increase of the turbulence level. In particular, turbulent bursts are originated at flow reversal when the vortex structures generated during the previous half-cycle are convected back and interact with the vorticity of opposite sign which is shed by the crests of the bottom forms. More recently, the oscillatory boundary layer over a rippled bed has been determined by means of a DNS by Ønder and Yuan (2019), who used the open-source code Nektar++, which is based on a finite element method (FEM) and employs elements of variable size.

Fig. 27 shows isosurfaces provided by the *Q*-criterion, which identifies the regions characterized by high values of vorticity. Since the viscous stresses are function of the strain rate only, positive values of $Q = \frac{1}{2}\left(\|\mathbf{O}\|^2 - \|\mathbf{D}\|^2\right)$, **D** and **O** being the symmetric and antisymmetric part of the velocity gradient tensor, are indicative of volumes where the vorticity dominates. On the other hand, negative values of Q characterize regions where the strain rate or the viscous stresses dominate.

Looking at Fig. 27, it can be observed that (i) a spanwise vortex is generated by the roll-up of the vorticity shed by the ripple crest and (ii) this coherent vortex is surrounded by vortex filaments which are generated by the stretching of residual vorticity patches.

Of course the computational resources that are required to make direct numerical simulations of the oscillatory boundary layer over a wavy bed are very high and rapidly increase with increasing values of the Reynolds number in such a way that the simulations of the flow at high Reynolds number become prohibitive.

High values of the Reynolds number can be handled more easily by means of the Large Eddy Simulation (LES) approach. The LES approach reduces the computational resources that are required by the DNS by

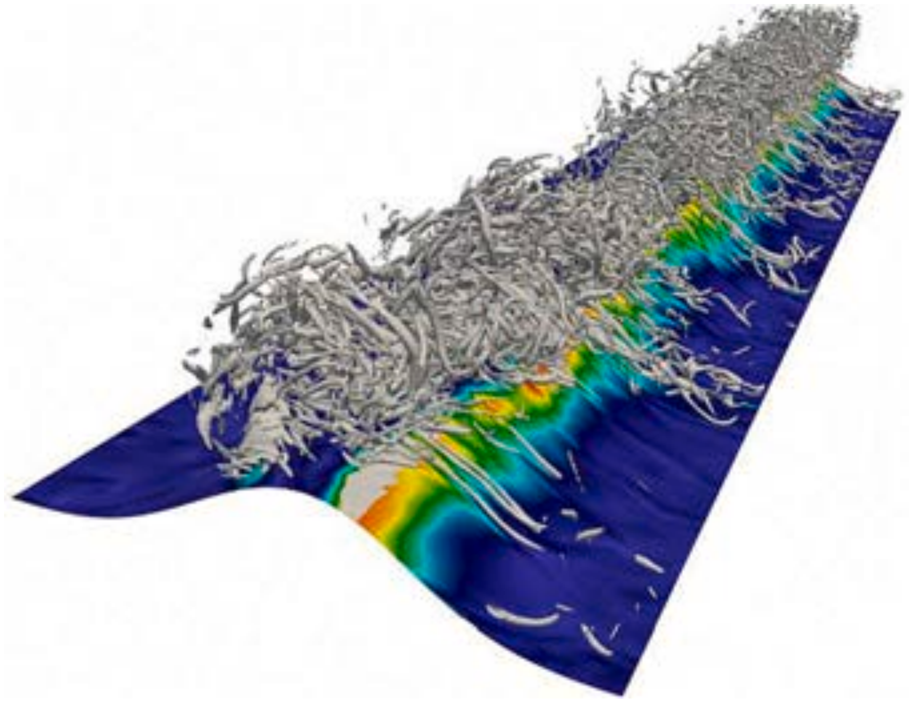

Fig. 27. Vortex structures generated by an oscillatory flow over a rippled bed and visualized by isosurfaces of the Q parameter. The flow was computed by means of Direct Numerical Simulations by Ønder and Yuan (2019) who simulated two cases characterized by (i) $R_\delta = 70.7, \frac{h_r}{\lambda_r} = 0.167, \frac{U_0 T}{\lambda_r} = 5.24$; (ii) $R_\delta = 141, \frac{h_r}{\lambda_r} = 0.167, \frac{U_0 T}{\lambda_r} = 5.24$ (courtesy of Asim Onder).

modelling the dynamics of the smallest vortex structures. The Navier-Stokes equations are filtered by using a low-pass filter. However, the effects of the small vortices, which are not explicitly solved by the numerical scheme, on the resolved flow field should be modelled by means of so-called subgrid scale models.

The turbulent boundary layer over a rippled bed was evaluated by using a LES approach also by Zedler and Street (2006) who coupled the study of the flow field to the evaluation of the sediment transport. The equations that were considered by Zedler and Street (2006) are the volume-filtered continuity and Navier-Stokes equations along with the volume-filtered advection-diffusion equation for sediment concentration. In particular, the SFS stresses are quantified by means of the dynamic mixed model of Zang et al. (1993). Moreover, the boundary condition for the velocity take into account the presence of a rough bottom. The SFS stress and scalar flux terms in the concentration equation are modelled by means of the same approach thus using the common assumption that the turbulent Schmidt number (ratio between the eddy viscosity and the eddy diffusivity) is equal to 1. The scale similarity (Bardina et al. (1983)) term is computed separately for the two equations. The pick-up rate of the sediment from the bottom is evaluated by means of van Rijn (1984)'s empirical function, which provides the pick-up rate as a function of the Shields parameter (ratio between the bottom shear stress and the quantity $(\rho_s - \rho)gd$). The results show that, although the main vortex structures generated by boundary layer separation at the ripple crest are two-dimensional, the flow becomes rapidly three-dimensional.

Chou and Fringer, 2010 used the large eddy simulation of the oscillatory flow over a wavy wall to simulate the dynamics of the bottom profile. In order to follow the time development of profile of the bottom, the hydrodynamic problem was solved by introducing a moving curvilinear coordinate system fitted to the boundary. While the largest vortex structures are solved by the numerical procedure, the smallest vortices are modelled by introducing a dynamic mixed model. Fig. 28 shows the time development of the vortex structures generated by an oscillatory flow over a rippled bed as computed by Chou and Fringer (2010).

To solve the advection-diffusion equation for the sediment concentration c, Chou and Fringer (2010) used an empirical relationship to quantify the sediment pick-up rate at the bottom. Then, they combined the suspended load with the bed load and determined the time development of the bottom profile using Exner equation and taking into account the gravity-induced avalanche sediment transport, i.e. the local flux of sediment which takes place when the local bottom slope becomes larger than the angle of repose of the sediment. Hence, in their work, the time development of the bottom profile affects the hydrodynamics in a coupled simulation and the bottom features evolve because of the resolved turbulent flow.

LES of the oscillatory flow over a rippled bed, coupled with the evaluation of the time development of the bottom profile, were carried out by Leftheriotis and Dimas (2016) who forced the no-slip condition at the bottom by using the immersed boundary method. The time development of the bedforms was obtained by numerically integrating sediment continuity equation (Exner equation) and considering the flow averaged in the spanwise direction. The code by Leftheriotis and Dimas (2016) was able to simulate the appearance of ripples from a quasi-flat bed and to follow their time development. The numerical model predicts ripple wavelengths that agree with those predicted by empirical formulae. Moreover, as it can be seen in Fig. 29, the geometrical characteristics of ripples turn out to be independent of the form of the initial perturbation. Further Large Eddy Simulations have recently been performed by Chalmoukis et al. (2020), Jin et al. (2021), Jin et al. (2022).

Since the ripples induced on a cohesionless bottom by an oscillatory flow are characterized by straight crests at equilibrium but they develop transient three-dimensional geometries when moving from one equilibrium state to another equilibrium state because of the change of the external forcing flow, Chalmoukis et al. (2020) performed LES of the oscillatory flow over three-dimensional, fixed wavy bed. The objective of their simulations was to determine the intercorrelation between the flow dynamics and the evolution of the defects of the bedforms that move from a two-dimensional equilibrium to another two-dimensional bottom configuration. In particular, Chalmoukis et al. (2020)

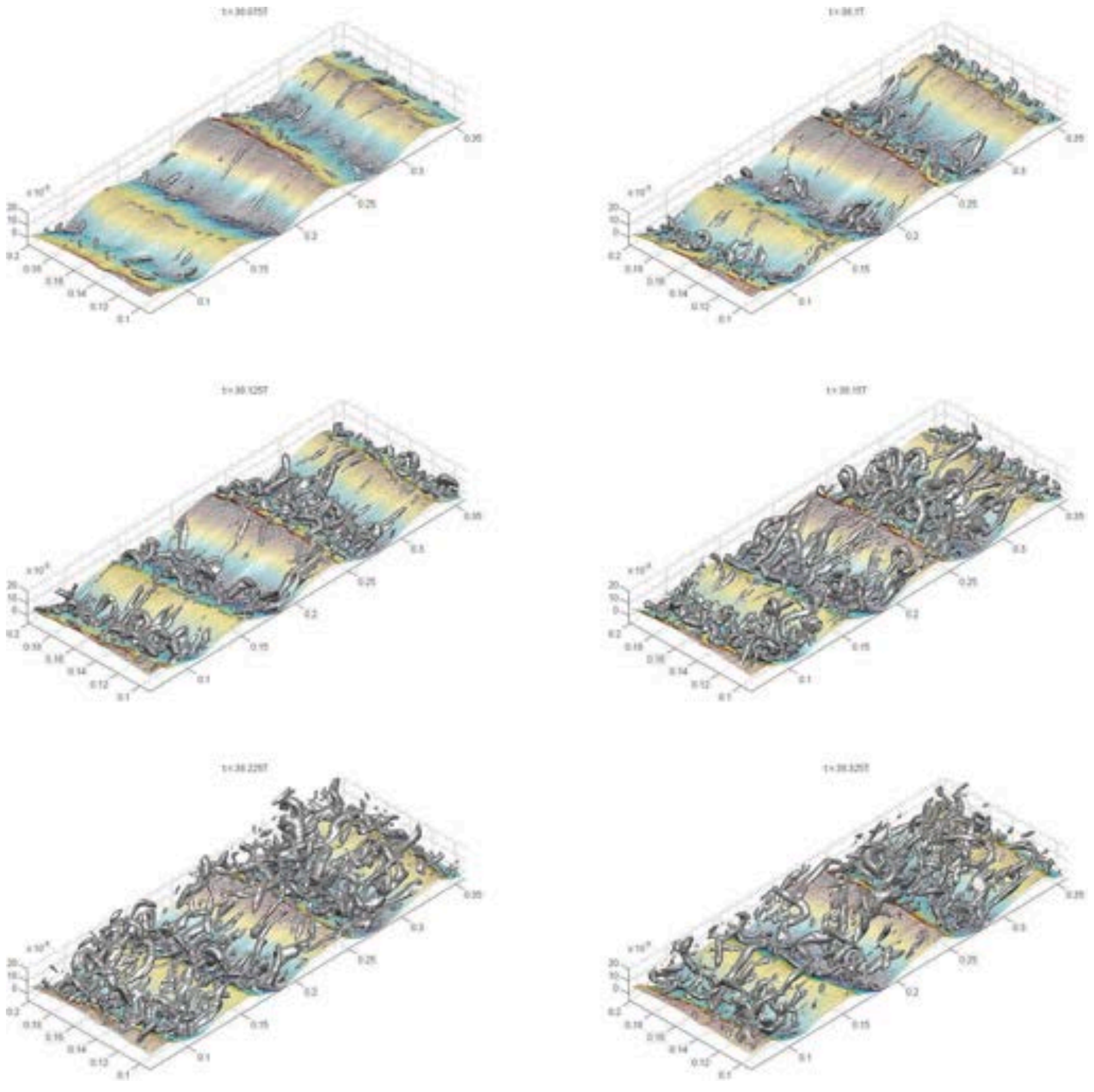

Fig. 28. Vortex structures generated by an oscillatory flow over a rippled bed computed by means of a Large Eddy Simulation approach (Chou and Fringer (2010)), $R_\delta \simeq 640$, $\frac{d}{\delta} \simeq 0.17$ (courtesy of Yi-Ju Chou and Oliver Fringer).

simulated the flow over a ripple characterized by a sinusoidal crest surrounded by other regular ripples characterized by straight crests. The sinusoidal crest introduces slope asymmetries on opposite sides of the crest, and Chalmoukis et al. (2020) found that steep-sloped regions generate thicker recirculation areas, whereas in the more gently-sloped regions the recirculation regions are thinner. Moreover, streamwise vortical structures appears close to the sinusoidal crest. These vortex structures might be responsible for the gradual reformation of the rippled bed, as they induce strong bed shear stresses and, hence, large sediment transport rates and rapid changes of the bottom profile.

Jin et al. (2021) performed a high-resolution LES of the oscillatory flow over a sinusoidal ripple-like bedform and validated the code both qualitatively and quantitatively by comparing the numerical results with previous laboratory experiments and numerical simulations. In particular, Jin et al. (2021) analysed the dynamics of the “ribs”, strong vortex structures that develop perpendicular to the crests of the bedforms. They showed that the ribs tend to appear either on the up-slope or the down-slope side of the ripple with a different spacing which ranges from $\frac{\lambda_r}{8}$ up to λ_r, depending on the accelerating/decelerating phases of the cycle. The presence of these three-dimensional vortex structures induces a large variability of the shear stress in the spanwise direction, which could favour the development of three-dimensional beforms. Since in the field the crests of the ripples are not necessarily straight and continuous and the bottom forms present irregularities called ‘defects’, Jin et al. (2022) performed high-resolution LES to investigate the flow field over both regular and irregular ripples. In particular, they

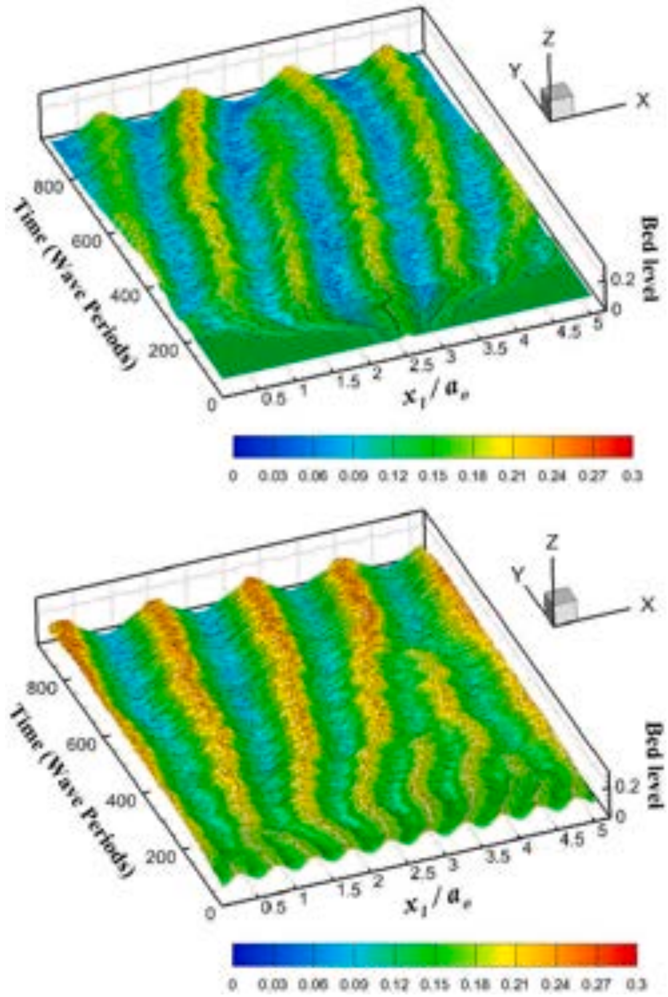

Fig. 29. Ripple appearance on a flat bottom forced by an oscillatory flow. In the figure the streamwise coordinate is made dimensionless by using the amplitude a_0 of the fluid oscillation in the irrotational region. The sediment mobility number ψ_d is equal to 20 and the Reynolds number R_δ is about 140. Top panel: the ripples appear from an initial localized perturbation. Bottom panel: the ripples appear from a periodic bottom perturbation of small wavelength. Adapted from Leftheriotis and Dimas (2016) (courtesy of Athanassios Dimas).

considered two different types of ripple irregularities, i.e. ripples with a termination defect and ripples with a bifurcation defect. When the results for irregular ripples are compared with those obtained for regular ripples, as expected, Jin et al. (2022) found that the maximum velocity, the vortex strength and the position of the vortex center over the ripples close to the bottom irregularity are all affected by the presence of the defect.

A significant reduction of the computational costs can be achieved by considering the Reynolds averaged equations and determining only the ensemble averaged values of the velocity and pressure fields. Indeed, in the turbulent regime, velocity and pressure can be decomposed into two parts: an average value and a fluctuating contribution. The time development of the former contribution is described by the Reynolds averaged equations which, however, require a turbulence model to be closed. In fact, the Reynolds stresses generated by the nonlinear terms of Navier-Stokes equations, should be related to the mean flow thus removing any reference to the fluctuating part of the velocity. Of course, turbulence models of different complexity can be used to model the Reynolds stresses, starting from simple algebraic models to more complex two-equation models.

Andersen (1999) modelled turbulence over two-dimensional ripples by means of a Boussinesq approach and a two-equation closure model (Wilcox (1988), Wilcox (1993)) and coupled the study of the flow with that of the bottom development. Sediment transport was split into bed load and suspended load components. The former was computed by means of an empirical relationship, whereas the suspended load was determined by solving the advection-diffusion equation for the sediment concentration. Andersen (1999) carried out simulations of several ripples and was able to reproduce both the appearance of ripples and their disappearance.

More recently, Marieu et al. (2008) modelled the Reynolds stresses by means of the two-equation turbulence model by Wilcox (1988), which describes turbulence dynamics by evaluating the spatial and temporal development of k (the turbulent kinetic energy) and ω_t (the turbulent vorticity). The time development of the bottom was numerically determined by quantifying both the bed load and the suspended load and by using Exner (sediment continuity) equation. Marieu et al. (2008) were able to simulate the ripple growth from an almost flat bed showing that the ripples reach an equilibrium when the flux of sediment due to local avalanches balances the trend of the sediment to pile up at the ripple crests. In particular, the model by Marieu et al. (2008) was able to simulate ripple creation, growth, merging and disappearance. Sishah and Vittori (2022) used the $k-\omega$-SST model by Menter et al. (2003) and computed the flow over vortex ripples for large values of R_δ. As in Blondeaux and Vittori (1991c), they observed that, for large values of the ratio between the fluid excursion and the ripple wavelength, the vortex shed on one side of the ripple crest when the external velocity is positive is no longer the mirror image of the vortex shed on the other side when the external flow reverses its direction and the dynamics of the vortex structures become quite complex. Moreover, a horizontal steady streaming is generated in the positive/negative direction depending on the initial conditions.

Chen and Yu (2015) evaluated the time development of the ripples by using a two-phase flow model that considers the Reynolds-averaged momentum and continuity equations for both the fluid and sediment phases. It is worth pointing out that the model by Chen and Yu (2015) can be applied over the whole depth from the undisturbed sandy bed, where the sediment grains are at rest, up to the low concentration region far from the ripples. Moreover, neither a reference concentration nor a pickup function are required and there is no need to distinguish between the bed load and the suspended load since these empirical information are replaced by the interphase model. The results by Chen and Yu (2015), which are supported by a reasonable agreement with laboratory data, show that the two-phase flow model can well describe the formation-ejection process of vortices from the crests of the ripples as well as the trapping-lifting process of sediments by these vortex structures. Further studies of ripple dynamics using a two-phase flow model were carried out by Salimi-Tarazouj et al. (2021) who determined the evolution of ripple geometries due to different wave forcing parameters. In particular Salimi-Tarazouj et al. (2021) made a series of numerical experiments and determined the response of the ripple bed to a step-change in the forcing waves simulating ripple ‘splitting’, ‘sliding’, ‘merging’ and ‘protruding’ as the bedforms evolve to a new equilibrium.

Even though the numerical simulations of the processes taking place close to a rippled bed are continuously improving, detailed experimental informations are required both to validate the models and to gain a more complete picture of the phenomenon.

Earnshaw et al. (1995) used the particle image velocimetry (PIV) to visualize the largest vortex structures, thus providing data that can be used to test the results obtained by means of large eddy simulation. Yoshikawa et al. (2004) measured the velocity field within the oscillatory boundary layer over a wavy bottom characterized by gentle slopes (rolling-grain ripples). Yoshikawa et al. (2004) were able to visualize the flow structures and in particular the transient recirculating cells, which are generated by an oscillatory flow above naturally formed rolling-grain ripples. The evolution of the flow structures turned out to be in agreement with the results of the theoretical investigations based on the assumption of small ripple amplitudes. Later, Rousseaux (2008) used the same experimental technique to measure the oscillatory flow over vortex ripples focussing his attention mainly on the vorticity dynamics and the existence of steady recirculating cells (see Fig. 30). The results by Rousseaux (2008) show the shedding of a vortex structure every half oscillatory cycle and the generation of a jet when the vortex structure is convected back by the external flow and passes over the crest of the ripple.

The increasing power of actual computer has recently allowed the evaluation of the dynamics of the ripples by considering the dynamics of each sediment grain and the flow around each particle (Mazzuoli et al., 2024). An example of the results is shown in Fig. 31.

4.5.3. *Time-varying bedforms and hysteresis effects*

Of course, the bedform characteristics change over time from their appearance till their equilibrium geometry is attained. As pointed out by Perillo et al. (2014a), understanding the morphological time development of the bedforms is important for the reconstruction of ancient sedimentary records. Hence, Perillo et al. (2014a) made laboratory experiments to investigate the time development of the ripples under purely unidirectional, oscillatory and combined-flow conditions. Their results show that the appearance and growth of the bedforms are similar for all types of forcing flows and are characterized by four stages: (i) incipient bedforms; (ii) growing bedforms; (iii) stabilizing bedforms; and (iv) fully developed bedforms. Moreover, the time development of the bedforms exhibits the same general trend for different flow types independently from the bedform size, the bedform shape and geometry (for example, two-dimensional versus three-dimensional bedforms), the flow velocity and the sediment size. Perillo et al. (2014b) made a similar experimental investigation on the initiation of bedforms from an artificially generated defect on a flat bed under unidirectional, oscillatory, and combined flows to obtain a quantitative insight into the process that leads to the appearance of the bedforms. In particular Perillo et al. (2014b) used a time-lapse photography tecnique that allowed to obtain the time development of the downstream and upstream edges of the defects.

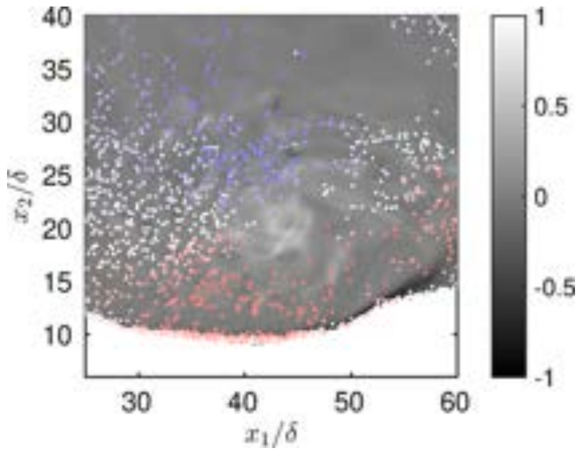

Fig. 31. Enlarged visualization of the vorticity field generated by the oscillatory flow over a rippled bed and of the position of the sediment particles picked-up from the bottom at $t/T = 19/20$. The vorticity is scaled with the angular frequency ω of the velocity oscillations of the fluid far from the bottom. The particles are coloured by their streamwise velocity (red: positive values; blue: negative values; white: particles with almost zero speed) and the gray bar on the right hand side of the panel indicates the vorticity strength that is scaled with the angular frequancy ω ($U_0/\omega = 8.0$ cm, $T = 2$ s, $\rho_s/\rho = 2.65$, $d = 0.28$) (courtesy of Marco Mazzuoli). (For interpretation of the references to colour in this figure legend, the reader is referred to the web version of this article.)

Testik et al. (2005) made a laboratory investigation on the characteristics of ripples under changing wave conditions. They considered waves of small, moderate, and large amplitudes named $S-$, $M-$ and $L-$ waves, respectively, and simulated three different cases of cyclic variation of wave amplitude, i.e. the $M-L-M$ cycle, the $L-M-L$ cycle and the $L-S-L$ cycle. Testik et al. (2005) observed three main

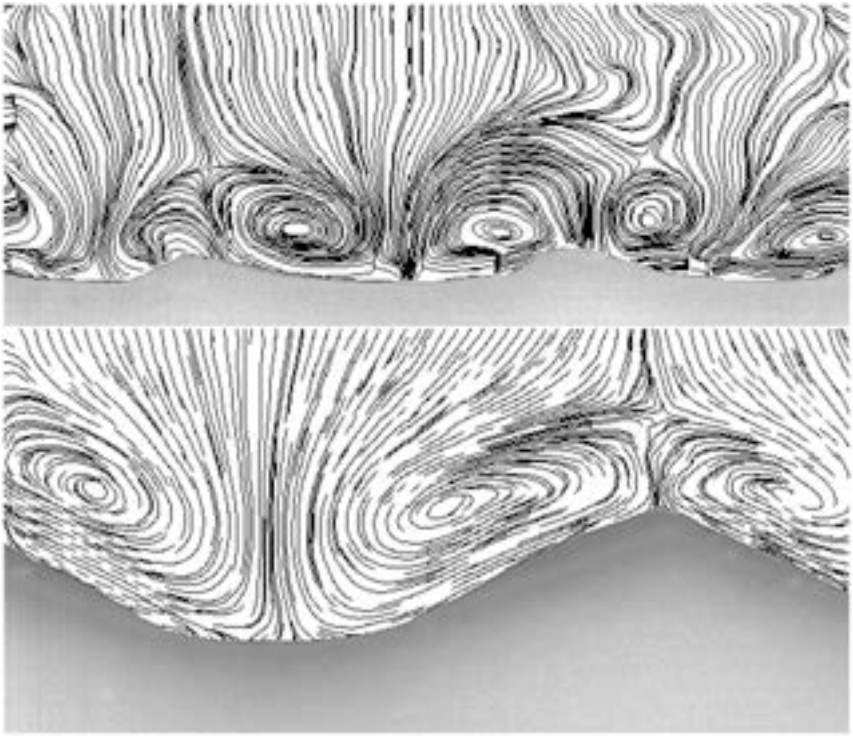

Fig. 30. Experimental streamlines of the oscillatory flow over a rippled bed averaged over a period. Top panel: rolling grain ripples, bottom panel: vortex ripples (courtesy of Germain Rousseaux).

different processes of the ripple adjustment to a new forcing flow: ripple splitting, ripple regrowth, and ripple flattening. For example, when the forcing waves are decreased from $L-$ waves to to $M-$ waves, the wavelength of the ripples also decreases and it attains a new equilibrium. Then, when the amplitude of the forcing waves is increased back to its original value, the wavelength of the ripples returns back to its original value. On the other hand, during the $L-S-L$ cycle, when the amplitude of the forcing flow decreases from the large value to the small value, the crests of the ripples are flattened but their wavelength appears to be constant. Then, when the amplitude of the forcing waves takes its original value, the height of the ripples grows back to its initial value, the wavelength of the ripples being essentially unaffected by the change of the forcing waves.

Also Nienhuis et al. (2014) made laboratory experiments to observe ripple dynamics under changing forcing waves. They observed ripples that are characterized by a uniform wavelength at equilibrium and develop defects when they respond to changes of the forcing waves. When the amplitude of the water oscillations close to the sandy bed is decreased significantly, two new incipient crests appear in every ripple trough, but only one incipient crest grows into a new full-sized crest. It is intersting to point out that the visualizations showed that the same incipient crest (the right or the left incipient crest) prevails in every trough thus showing that the dynamics of a ripple affects the adjacent ripples. The experiments also showed that, when the amplitude of the fluid oscillations increases, the ripple crests become sinuous and eventually break up giving rise to a three-dimensional bottom configuration.

Jin et al. (2019) made a series of laboratory experiments to investigate the appearance and development of ripples under varying conditions. In particular Jin et al. (2019) measured the rate of ripple adjustment and the mean ripple wavelength both before and after the change in the wave forcing. They showed that an increase of the wave forcing leads to a faster growth of the ripples and a longer final wavelength. A decrease of the wave forcing leads to a shorter wavelength of the ripples. Moreover, they observed hysteresis phenomena. Jin et al. (2019) investigated also the role of the initial perturbation on the growth rate and final geometry of the ripples. A larger amplitude of the initial perturbation leads to a faster growth of ripples and a larger ripple wavelength.

Of course, experimental data are essential to understand the dynamics of ripples under a varying wave forcing. However, equally important is the availability of formulas able to predict the temporal evolution of the ripple geometry (Soulsby et al. (2012)).

Of course, when the amplitude of the velocity oscillations close to the bottom is smaller than the threshold value for sediment motion, the sediments do not move and pre-existing ripples remain unchanged (relic ripples). On the other hand, when the amplitude of the velocity oscillations is larger than the threshold value for sediment motion, the ripple height and wavelength change and their time development should be predicted for any time-series of heights and periods of the surface waves. As pointed out by Soulsby et al. (2012), the experimental investigations show that, following a step change in the driving waves, the time development of the ripple height $h_r(t)$, from an initial value h_{r0} to a new equilibrium value $h_{r,eq}$, can be described by an exponential relaxation given by

$$\frac{h_r}{h_{r,eq}} = 1 - \left[1 - \frac{h_{r0}}{h_{r,eq}}\right] exp\left(-\frac{\beta t}{T_e}\right) \tag{27}$$

where T_e is a characteristic time scale of the phenomenon and β is a coefficient that governs the rate of change. A more general expression, better suited to application to constantly varying field conditions, is provided by the following ordinary differential equation

$$\frac{dh_r}{dt} = \frac{\beta}{T_e}\left(h_{r,eq} - h_r\right) \tag{28}$$

It is worth pointing out that Eq. (27) is a solution of Eq. (28) only if $h_r = h_{r0}$ at $t = 0$ and β, T_e and $h_{r,eq}$ are time independent. Similar equations can be used to describe the time-varying ripple wavelength $\lambda_r(t)$, since also the wavelength was observed to follow an exponential relaxation. The characteristic time scale T_e can be assumed to be the wave period, i.e. $T_e = T$, and Soulsby et al. (2012) proposed to evaluate β by means of

$$\beta = 2.996\frac{\psi_d^{1.07}}{21,700 + \psi_d^{1.07}} \tag{29}$$

5. Genetic programming to predict ripple characteristics

In the last years, the use of artificial intelligence has become widespread to solve any kind of problem and, in artificial intelligence, genetic programming is an approach that mimic the natural process to select a program to solve a particular problem.

Goldstein et al. (2013) used genetic programming, to obtain a predictor for the wavelength and the height of ripples. In particular, Goldstein et al. (2013) trained their genetic algorithm with data selected using a maximum dissimilarity selection routine that allowed them to use less data for the training of their software and more data to test the results. They obtained a smooth and physically meaningful predictor that shows that the ripple wavelength is a weakly nonlinear function of both the grain size and the fluid orbital excursion close to the bottom. When the predictions are compared with the results of other ripple predictors, Goldstein et al. (2013) found that their results are characterized by a lower normalized root mean squared error thus showing that the machine learning techniques can be successfully used to develop a good ripple predictor, if a large data set is available. However, as pointed out by Goldstein et al. (2013) themselves, the new predictor does not consider i) the details of ripple shape (which is assumed to be characterized only by a characteristic length and a characteristic height), ii) the possible presence of three dimensional ripples, iii) heterogeneous sediments, iv) the possible presence of a steady current, v) the effects of biota and vi) hysteresis effects. These limitations are widely discussed by Goldstein et al. (2013) but it is important to note that also the other existing ripple predictors capture one or more of these processes but not all.

6. Migrating ripples

When a steady current is superimposed to propagating surface waves, the so-called wave-current ripples are observed, the characteristics of which fall between those of the ripples generated by a pure oscillatory flow and those of the current ripples described a.o. by Vittori and Blondeaux (2022). Since the flow generated close to the bottom by sea waves is characterized by an oscillatory velocity component plus a steady velocity component originated by nonlinear, second-order effects (Longuet-Higgins (1953)), the ripples generated by surface waves characterized by large amplitudes have geometrical and kinematical characteristics that are somewhat similar to those of the ripples generated by the interaction between a wave of quite small amplitude and a steady current. In particular, the ripples migrate in the direction of the steady velocity component.

The distinguishing geometric characteristic of wave-current ripples and that of the ripples generated by large amplitude waves is the asymmetry of their profile. In Fig. 7 the symmetry index of ripples (we remind that the symmetry index is defined as the ratio $\frac{l_2}{l_1}$ between the length l_2 of the gentle (up-current) side to the length l_1 of the steep (down-current) side of the ripples) is plotted versus the ratio between the steady velocity component u_s and the maximum near-bed orbital velocity U_0, which are evaluated just outside the bottom boundary layer. When the steady velocity component is generated only by the propagation of a surface wave, the value of u_s is evaluated according to the theory of Longuet-Higgins (1953).

Not much is known theoretically on wave-current ripples and the available results are mainly for the asymmetric ripples generated by sea waves of large amplitude. Blondeaux et al. (2000) and Blondeaux et al. (2015) investigated the effect that the steady streaming generated by propagating surface waves has on the formation of ripples by means of a linear stability analysis and determined the symmetry index and the migration speed of the bedforms as function of the hydrodynamic and morphodynamic parameters of the problem.

Fig. 32, where the experimental data are plotted along with the theoretical predictions of Blondeaux et al. (2000) and Blondeaux et al. (2015), shows that the ripples become more asymmetric as the steady velocity component increases. Moreover, comparing the data of wave-current and current ripples with those of wave ripples, it can be observed that a unidirectional current unrelated to waves affects ripple asymmetry in much the same way as wave-induced mass-transport.

Blondeaux et al. (2000) evaluated also the migration speed of the ripples and compared the theoretical results with experimental measurements. Since the theoretical values depends on the formula used to estimate the sediment transport rate, Blondeaux et al. (2000) obtained results using both the formula of Hallermeier (1982) and that of Sleath, 1984. A comparison between the theoretical and experimental values of the quantity $\frac{G_{1i}}{\alpha}$, that is proportional to the migration speed of the ripples, is shown in Fig. 33.

Even though the theoretical analyses of Blondeaux et al. (2000) and Blondeaux et al. (2015) assume the flow regime in the bottom boundary layer to be laminar and the results are strictly valid only for ripples at the initial stage of their formation or for mature ripples of small amplitude (rolling-grain ripples), the comparison of the theoretical findings with laboratory measurements seems to suggest that the theoretical analyses capture the main ingredients of the phenomenon of ripple migration. However the reader should consider that, when the amplitude of the bottom forms grows and the ratio between the height and the length of the bottom forms becomes larger than a critical value ranging about 0.17 (Sleath (1984)), the bottom boundary separates from the crests of the ripples, rolls up and generates vortex structures which make the linear analysis inappropriate. Hence the agreement appears to be largely fortuitous.

7. Conclusions and possible future developments

When the local water depth is smaller than half the length of the surface wave and the bottom is made up of cohesionless sediments, the surface wave can give rise to the formation of bedforms characterized by a length that is of the order of magnitude of the amplitude of the water particle oscillations close to the bottom, i.e. a length of the order of tens of centimetres. Even though different bottom profiles are observed (e.g. two-dimensional ripples, brick-pattern ripples, tile ripples, …), in practical applications characterized by a large spatial scale, ripples are often considered just as a bottom roughness the size of which can be determined by means of empirical predictors. If a detailed knowledge of the flow within the bottom boundary layer is required, the appearance of ripples and their geometrical characteristics can be predicted by means of stability analyses that are briefly summarized herein along with the results they provide. A comparison of the theoretical predictions with laboratory measurements seems to support the results of the stability analyses. Indeed, the linear and weakly nonlinear stability analyses provide fair predictions of the size of the ripples and of their plane view but their equilibrium amplitude can be predicted only taking into account strong nonlinear effects that call for numerical approaches. The predictions of the stability analyses are considered 'fair' because the uncertainty of the predictors of the sediment transport rate makes it difficult to obtain accurate results but the stability analyses can describe the main characteristics of the ripples as function of the hydrodynamic and morphodynamic parameters of the problem. Moreover, the stability analyses commonly require the flow regime in the bottom boundary layer to be laminar. However, often turbulence appears being triggered also by the bottom roughness. Hence, the stability analyses should be extended to cover also the turbulent regime. Only the analysis of Foti and Blondeaux (1995b) considers the turbulent regime but the Reynolds equations are closed by means of a very simple turbulence model. Taking into account that the actual turbulence models (e.g. the two-equaton turbulence model $e-\omega$) provide a reliable descrition of turbulence dynamics, to improve the predictions of bedform characteristics, their use is desirable. Moreover, further efforts should be made to refine the actual predictors of the sediment transport rate generated by the flow due to the interaction of a steady current with a propagating surface wave and to refine the description of the effects that the local bed slope has on sediment dynamics. Recently, attempts have been made to quantify the sediment transport rate and to determine the time development of bottom forms by means of direct numerical simulations (DNS), to evaluate the fluid motion, and discrete element methods (DEM), to evaluate the trajectories of the sediment grains (e.g. Kidanemariam et al. (2013); Kidanemariam and Uhlmann (2014); Mazzuoli

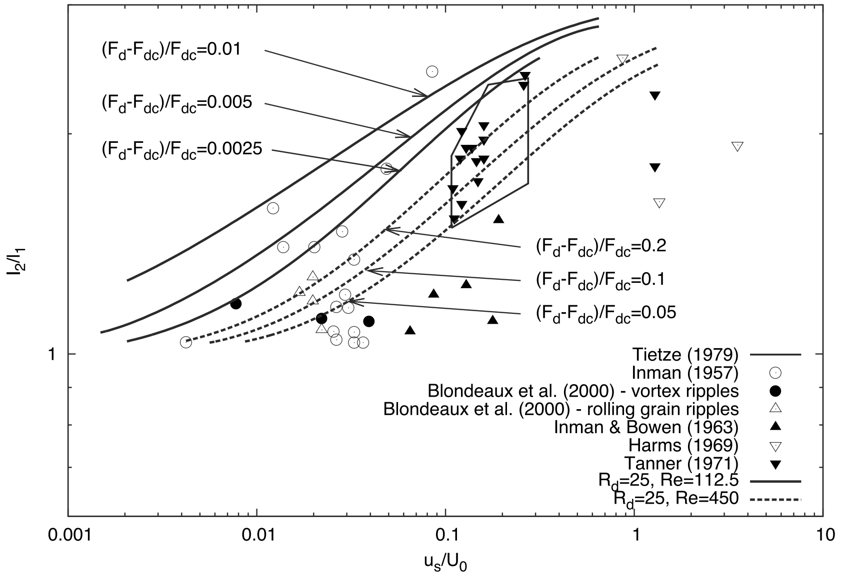

Fig. 32. Theoretical value of the symmetry index l_2/l_1 plotted versus u_s/U_0 along with the experimental measurements ($R_d = 25$ and $Re = 112.5, 450$ (or equivalently $R_\delta = 15, 30$) are the values of the Reynolds numbers of the experiments of Blondeaux et al. (2015)).

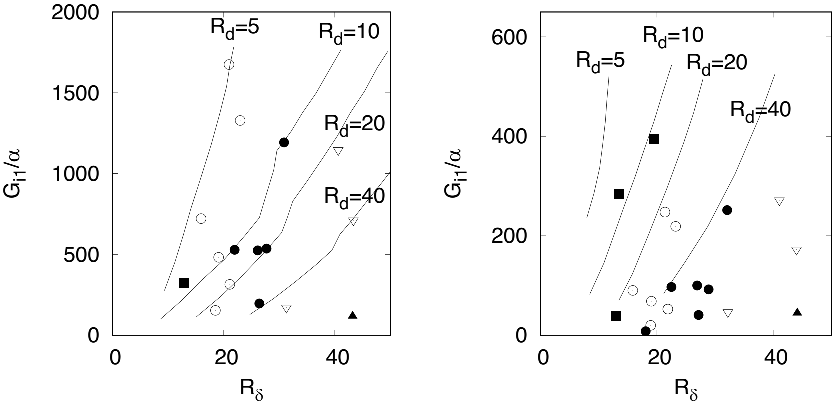

Fig. 33. Theoretical and experimental values of the quantity $\frac{G_{1i}}{\alpha}$, which is proportional to the migration speed of the ripple. The values plotted in panel (*a*) are computed by evaluating the sediment transport rate by means of the formula by Hallermeier (1982) whereas those plotted in panel (*b*) are obtained by means of the formula by Sleath (1984) (black squares, $5 < R_\delta < 10$, white circles, $10 < R_\delta < 15$, black circles, $15 < R_\delta < 20$, white triangles, $20 < R_\delta < 25$, black triangles, $25 < R_\delta < 30$.)

et al. (2016, 2019, 2020); Vittori et al. (2020b); Mazzuoli et al. (2022)). This approach can describe the details of flow around each sediment grain by solving Navier-Stokes and continuity equations and by forcing the no-slip condition at the surface of the grain. Hence, it is possible to evaluate the 'exact' values of the force and torque that the fluid exerts on each sediment grain and to compute its 'exact' trajectory by integrating Newton's laws. As shown in Figs. 31 and 35, where the vorticity field generated by an oscillatory flow over a rippled bottom made by cohesionless sediments is plotted at particular phases of the cycle along with the position of the sediments, this approach can describe i) the large vortex structures shed by the ripple crest, ii) the small turbulent eddies and iii) the dynamics of the sediments dragged by the flow. The results show that the large values of the bottom shear stress induced by the interaction of the coherent vortex structures with the bottom pick up a lot of sediments that are trapped within the bottom boundary layer and are dragged by the local velocity field. However, when the boundary layer separates from the bottom generating a free shear layer that rolls up and creates a large vortex, the sediments are ejected from the vortex core because of centrifugal effects. Even though this approach can describe the dynamics of both the large scale vortex structures as well as that of the small eddies shed by the sediment grains, it implies high computational costs and it cannot be used to describe large fluid domains. Moreover, to limit the computational costs, the sediment grains are assumed to have a spherical shape of uniform diameter *d*. Hence, it is not possible to describe the grain sorting process which is present when the bottom is made up of a mixture of sediments and ripples appear. For example, it is not possible to mimic the results by Foti and Blondeaux (1995a), who observed the ripples generated by an oscillatory flow over a sediment mixture characterized by a bimodal sediment distribution. Foti and Blondeaux (1995a) showed that the coarser fraction tends to oscillate around the crests of the bedforms while the finer fraction tends to move towards the troughs (see Fig. 34). Moreover, Foti and Blondeaux (1995a) observed also that the sorting phenomenon affects the dynamics of the ripples since the ripples generated by a well sorted sediment turn out to be shorter than those generated by a poorly sorted sediment.

However, the power of computers is continuously increasing and in a near future it will be possible to simulate the dynamics of a sediment mixture taking also into account the irregular shape of the sediment grains. For the moment, while the motion of the fluid phase is determined by solving Navier-Stokes and continuity equations, the motion of the sediment particles is often determined by means of a point-particle approach where appropriate closure relationships are introduced to evaluate the force and torque acting on the particles and to compute their trajectory. For example Finn et al. (2016) used a point particle approach to investigate sediment dynamics in an oscillatory flow over a rippled bed. However, it should be pointed out that this approach requires that the "disturbance" of the computed flow field due to the presence of a particle be smaller than the resolved flow scales. In other word, the point-particle approach requires that the particle size be significantly smaller than the grid-cell.

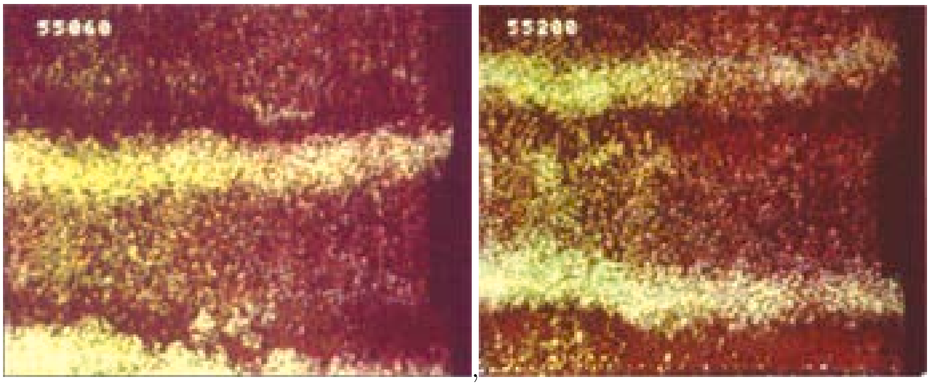

Fig. 34. Grain sorting over ripples. The yellow sediment grains are coarser that the red sediments and pile up at the crests of the ripples that are generated in a U-tube by an oscillatory flow. The figure shows a top view of the bottom at two different phases of the cycle (adapted from Foti and Blondeaux (1995a)). (For interpretation of the references to colour in this figure legend, the reader is referred to the web version of this article.)

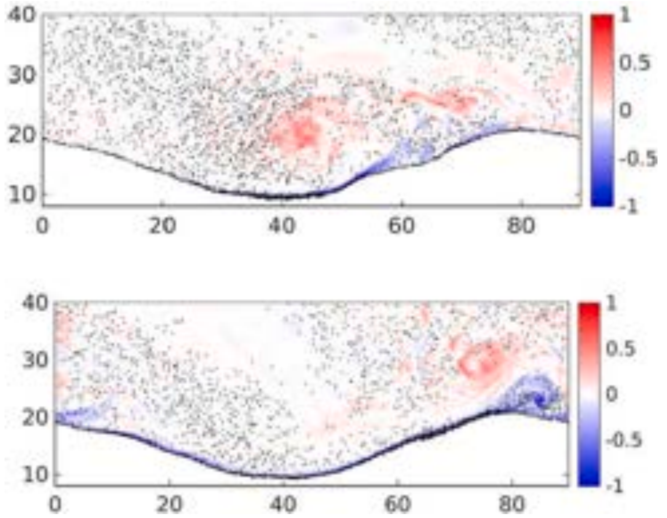

Fig. 35. Visualization of the vorticity field generated by the oscillatory flow over a rippled bed and the position of the sediment grains picked up from the bottom at $t = 2.4\pi$ (top panel) and $t = 2.6\pi$ (bottom panel) for $R_\delta = 201, R_p = 18.9, \frac{d}{\delta} = 0.35, s = 2.65$. The vorticity is scaled with the angular frequency ω of the velocity oscillations of the fluid far from the bottom (courtesy of Marco Mazzuoli).

Author contributions

All the authors contributed equally to analysing data, reaching conclusions and in writing the paper.

Declaration of competing interest

The authors report no conflict of interest.

Data availability

The authors do not have permission to share data.

Acknowledgments

This research was funded by the Ministry of Education, University and Research (MIUR) (Italy) in the framework of the project “FUNdamentals of BREAKing wave-induced boundary dynamics - FUNBREAK” (PRIN 2017 - 20172B7MY9).

References

Adams, J.C., 1991. Recent enhancements in mudpack, a multigrid software package for elliptic partial differential equations. Appl. Math. Comput. 43 (1), 79–93.

Allen, J.R.L., 1982. Sedimentary Structures, their Character and Physical Basis, Vol. 1. Elsevier.

Amos, C., Kassem, H., Friend, P., 2019. Ripple marks.

Andersen, K.H., 1999. Ripples beneath surface waves and topics in shell models of turbulence. PhD thesis.

Bardina, J., Ferziger, J.H., Reynolds, W.C., 1983. Improved turbulence models based on large eddy simulation of homogeneous incompressible turbulence. Report TF, 19.

Barr, B.C., Slinn, D.N., Pierro, T., Winters, K.B., 2004. Numerical simulation of turbulent, oscillatory flow over sand ripples. J. Geophys. Res. Oceans 109 (C9).

Blondeaux, P., 1990. Sand ripples under sea waves. Part 1. Ripple formation. J. Fluid Mech. 218, 1–17.

Blondeaux, Paolo, 2001. Mechanics of coastal forms. Annu. Rev. Fluid Mech. 33 (1), 339–370.

Blondeaux, P., Vittori, G., 1991a. Vorticity dynamics in an oscillatory flow over a rippled bed. J. Fluid Mech. 226, 257–289.

Blondeaux, P., Vittori, G., 1991b. Oscillatory flow and sediment motion over a rippled bed. In: Coastal Engineering Conference, Delft, The Netherlands, July 2-6, 1990, pp. 2186–2199.

Blondeaux, P., Vittori, G., 1991c. A route to chaos in an oscillatory flow: Feigenbaum scenario. Phys. Fluids A Fluid Dyn. 3 (11), 2492–2495.

Blondeaux, P., Vittori, G., 1999. Boundary layer and sediment dynamics under sea waves. Adv. Coast. Ocean Eng. 4, 133–190.

Blondeaux, P., Sleath, J.F.A., Vittori, G., 1988. Experimental data on sand ripples in an oscillatory flow. Rep 1, 88.

Blondeaux, P., Foti, E., Vittori, G., 2000. Migrating Sea ripples. Eur. J. Mech. B/Fluids 19 (2), 285–301.

Blondeaux, P., Foti, E., Vittori, G., 2015. A theoretical model of asymmetric wave ripples. Philos. Trans. R. Soc. A Math. Phys. Eng. Sci. 373 (2033), 20140112.

Bolla Pittaluga, M., Imran, J., 2014. A simple model for vertical profiles of velocity and suspended sediment concentration in straight and curved submarine channels. J. Geophys. Res. Earth 119 (3), 483–503.

Boyd, R., Forbes, D.L., Heffler, D.E., 1988. Time-sequence observations of wave-formed sand ripples on an ocean shoreface. Sedimentology 35 (3), 449–464.

Chalmoukis, I.A., Dimas, A.A., Grigoriadis, D.G.E., 2020. Large-eddy simulation of turbulent oscillatory flow over three-dimensional transient vortex ripple geometries in quasi-equilibrium. J. Geophys. Res. Earth 125 (8) e2019JF005451.

Chen, X., Yu, X., 2015. A numerical study on oscillatory flow-induced sediment motion over vortex ripples. J. Phys. Oceanogr. 45 (1), 228–246.

Chou, Y., Fringer, O.B., 2010. A model for the simulation of coupled flow-bed form evolution in turbulent flows. J. Geophys. Res. Oceans 115 (C10).

Clifton, H.E., 1987. Wave-Formed Sedimentary Structures—A Conceptual Model.

Clifton, H.E., Dingler, J.R., 1984. Wave-formed structures and paleoenvironmental reconstruction. Mar. Geol. 60 (1–4), 165–198.

Craik, A.D.D., 1971. Non-linear resonant instability in boundary layers. J. Fluid Mech. 50 (2), 393–413.

Darwin, G.H., 1883. I. on the formation of ripple-mark in sand. Proc. R. Soc. Lond. 36 (228–231), 18–43.

De Vriend, H., 2001. Long-term morphological prediction. In: River, Coastal and Estuarine Morphodynamics. Springer, pp. 163–190.

Earnshaw, H.C., Bruce, T., Greated, C.A., Easson, W.J., 1995. Piv measurements of oscillatory flow over a rippled bed. In: Coastal Engineering, 1994, pp. 1975–1982.

Engelund, F., Fredsoe, J., 1982. Sediment ripples and dunes. Annu. Rev. Fluid Mech. 14 (1), 13–37.

Finn, J.R., Li, M., Apte, S.V., 2016. Particle based modelling and simulation of natural sand dynamics in the wave bottom boundary layer. J. Fluid Mech. 796, 340–385.

Foti, E., Blondeaux, P., 1995a. Sea ripple formation: the heterogeneous sediment case. Coast. Eng. 25 (3–4), 237–253.

Foti, E., Blondeaux, P., 1995b. Sea ripple formation: the turbulent boundary layer case. Coast. Eng. 25 (3–4), 227–236.

Garotta, V., Bolla Pittaluga, M., Seminara, G., 2006. On the migration of tidal free bars. Phys. Fluids 18 (9), 096601.

Goldstein, Evan B., Coco, Giovanni, Brad, A., Murray., 2013. Prediction of wave ripple characteristics using genetic programming. Cont. Shelf Res. 71, 1–15.

Grasmeijer, B.T., 2002. Process-based cross-shore modelling of barred beaches. PhD thesis.

Grass, A.J., Ayoub, R.N.M., 1982. Bed load transport of fine sand by laminar and turbulent flow. In: Coastal Engineering, 1982, pp. 1589–1599.

Hall, P., 1984. On the stability of the unsteady boundary layer on a cylinder oscillating transversely in a viscous fluid. J. Fluid Mech. 146, 347–367.

Hallermeier, R.J., 1982. Oscillatory bedload transport: Data review and simple formulation. Cont. Shelf Res. 1 (2), 159–190.

Hanes, D.M., Alymov, V., Chang, Y.S., Jette, C., 2001. Wave-formed sand ripples at duck, North Carolina. J. Geophys. Res. Oceans 106 (C10), 22575–22592.

Hansen, E.A., Fredsøe, J., Deigaard, R., 1994. Distribution of suspended sediment over wave-generated ripples. J. Waterw. Port Coast. Ocean Eng. 120 (1), 37–55.

Hara, T., Mei, C.C., 1990a. Oscillating flows over periodic ripples. J. Fluid Mech. 211, 183–209.

Hara, T., Mei, C.C., 1990b. Centrifugal instability of an oscillatory flow over periodic ripples. J. Fluid Mech. 217, 1–32.

Harms, J.C., 1969. Hydraulic significance of some sand ripples. Geol. Soc. Am. Bull. 80 (3), 363–396.

Horikawa, K., Watanabe, A., 1968. Laboratory study on oscillatory boundary layer flow. Coast. Eng. Jpn. 11 (1), 13–28.

Inman, D.L., 1957. Wave Generated Ripples in Nearshore Sands. Technical Report 100. Corps of Engineers.

Inman, D.L., Bowen, A.J., 1962. Flume experiments on sand transport by waves and currents. Coast. Eng. Proc. 8 (11), 137–150.

Jin, C., Coco, G., Tinoco, R.O., Goldstein, E.B., Gong, Z., 2019. Laboratory experiments on the role of hysteresis, defect dynamics and initial perturbation on wave-generated ripple development. Estuar. Coast. Shelf Sci. 224, 142–153.

Jin, C., Coco, G., Tinoco, R.O., Ranjan, P., San Juan, J., Dutta, S., Friedrich, H., Gong, Z., 2021. Large eddy simulation of three-dimensional flow structures over wave-generated ripples. Earth Surf. Process. Landf. 46 (8), 1536–1548.

Jin, C., Coco, G., Tinoco, R.O., Ranjan, P., Gong, Z., Dutta, S., San Juan, J.E., Friedrich, H., 2022. High-resolution large eddy simulations of vortex dynamics over ripple defects under oscillatory flow. J. Geophys. Res. Earth 127 (3) e2021JF006328.

Kaneko, A., Honji, H., 1979. Double structures of steady streaming in the oscillatory viscous flow over a wavy wall. J. Fluid Mech. 93 (4), 727–736.

Kidanemariam, A.G., Uhlmann, M., 2014. Interface-resolved direct numerical simulation of the erosion of a sediment bed sheared by laminar channel flow. Int. J. Multiphase Flow 67, 174–188.

Kidanemariam, A.G., Chan-Braun, C., Doychev, T., Uhlmann, M., 2013. Direct numerical simulation of horizontal open channel flow with finite-size, heavy particles at low solid volume fraction. New J. Phys. 15 (2), 025031.

Komar, P.D., 1974. Oscillatory ripple marks and the evaluation of ancient wave conditions and environments. J. Sediment. Res. 44 (1), 169–180.

Leftheriotis, G.A., Dimas, A.A., 2016. Large eddy simulation of oscillatory flow, sediment transport and morphology evolution over ripples based on the immersed boundary method. In: The 26th International Ocean and Polar Engineering Conference. International Society of Offshore and Polar Engineers.

Longuet-Higgins, M.S., 1953. Mass transport in water waves. Phil. Trans. R. Soc. Lond. Ser. A Math. Phys. Sci. 245 (903), 535–581.

Longuet-Higgins, M.S., 1981. Oscillating flow over steep sand ripples. J. Fluid Mech. 107, 1–35.

Luchi, R., Bolla Pittaluga, M., Seminara, G., 2012. Spatial width oscillations in meandering rivers at equilibrium. Water Resour. Res. 48 (5).

Lyne, W.H., 1971. Unsteady viscous flow over a wavy wall. J. Fluid Mech. 50 (1), 33–48.

Manohar, M., 1955. Mechanics of Bottom Sediment Movement Due to Wave Action.

Marieu, V., Bonneton, P., Foster, D.L., Ardhuin, F., 2008. Modeling of vortex ripple morphodynamics. J. Geophys. Res. Oceans 113 (C9).

Mazzuoli, M., Vittori, G., 2019. Turbulent spots in an oscillatory flow over a rough wall. Eur. J. Mech. B/Fluids 78, 161–168.

Mazzuoli, M., Vittori, G., Blondeaux, P., 2011. Turbulent spots in oscillatory boundary layers. J. Fluid Mech. 685, 365–376.

Mazzuoli, M., Kidanemariam, A.G., Blondeaux, P., Vittori, G., Uhlmann, M., 2016. On the formation of sediment chains in an oscillatory boundary layer. J. Fluid Mech. 789, 461–480.

Mazzuoli, M., Blondeaux, P., Simeonov, J., Calantoni, J., 2018. Direct numerical simulation of oscillatory flow over a wavy, rough, and permeable bottom. J. Geophys. Res. Oceans 123 (3), 1595–1611.

Mazzuoli, M., Kidanemariam, A.G., Uhlmann, M., 2019. Direct numerical simulations of ripples in an oscillatory flow. J. Fluid Mech. 863, 572–600.

Mazzuoli, M., Blondeaux, P., Vittori, G., Uhlmann, M., Simeonov, J., Calantoni, J., 2020. Interface-resolved direct numerical simulations of sediment transport in a turbulent oscillatory boundary layer. J. Fluid Mech. 885, A28.

Mazzuoli, M., Vittori, G., Blondeaux, P., 2022. The dynamics of sliding, rolling and saltating sediments in oscillatory flows. Eur. J. Mech. B/Fluids 94, 246–262.

Mazzuoli, M., Vittori, G., Blondeaux, P., 2024. Particle-resolved direct numerical simulation of the oscillatory flow and sediment motion over a rippled bed. Int. J. Multiphase Flow 172, 104707.

Mei, C.C., Liu, P.L.F., 1993. Surface Waves and Coastal Dynamics.

Menter, F.R., Kuntz, M., Langtry, R., et al., 2003. Ten years of industrial experience with the sst turbulence model. Turbul. Heat Mass Transfer 4 (1), 625–632.

Miller, M.C., Komar, P.D., 1980. A field investigation of the relationship between oscillation ripple spacinng and the near-bottom water orbital motions. J. Sediment. Res. 50 (1), 183–191.

Nayfeh, A.H., 2011. Introduction to Perturbation Techniques. John Wiley & Sons.

Nelson, T.R., Voulgaris, G., Traykovski, P., 2013. Predicting wave-induced ripple equilibrium geometry. J. Geophys. Res. Oceans 118 (6), 3202–3220.

Nielsen, P., 1981. Dynamics and geometry of wave-generated ripples. J. Geophys. Res. Oceans 86 (C7), 6467–6472.

Nielsen, P., 1992. Coastal Bottom Boundary Layers and Sediment Transport, 4. World scientific.

Nienhuis, Jaap H., Taylor Perron, J., Kao, Justin C.T., Myrow, Paul M., 2014. Wavelength selection and symmetry breaking in orbital wave ripples. J. Geophys. Res. Earth 119 (10), 2239–2257.

Ønder, A., Yuan, J., 2019. Turbulent dynamics of sinusoidal oscillatory flow over a wavy bottom. J. Fluid Mech. 858, 264–314.

Perillo, M.M., Best, J.L., Yokokawa, M., Sekiguchi, T., Takagawa, T., Garcia, M.H., 2014a. A unified model for bedform development and equilibrium under unidirectional, oscillatory and combined-flows. Sedimentology 61 (7), 2063–2085.

Perillo, M.M., Prokocki, E.W., Best, J.L., Garcia, M.H., 2014b. Bed form genesis from bed defects under unidirectional, oscillatory, and combined flows. J. Geophys. Res. Earth 119 (12), 2635–2652.

van Rijn, L.C., 1984. Sediment transport, part III: bed forms and alluvial roughness. J. Hydraul. Eng. 110 (12), 1733–1754.

Roos, P.C., Blondeaux, P., 2001. Sand ripples under sea waves. Part 4. Tile ripple formation. J. Fluid Mech. 447, 227.

Roos, P.C., Blondeaux, P., Hulscher, S.J.M.H., Vittori, G., 2005. Linear evolution of sandwave packets. J. Geophys. Res. Earth 110 (F4).

Rousseaux, G., 2008. Flow visualization and piv analysis over vortex ripples. In: ISFV13. 13th Unt. Symp. Flow Visualization (FLUVISU12). 12th French Congr. Visualization in Fluid Mechanics. Citeseer, Nice, France.

Saffman, P.G., 1995. Vortex Dynamics. Cambridge university press.

Salimi-Tarazouj, A., Hsu, T., Traykovski, P., Chauchat, J., 2021. Eulerian two-phase model reveals the importance of wave period in ripple evolution and equilibrium geometry. J. Geophys. Res. Earth 126 (7) e2021JF006132.

Scandura, P., Vittori, G., Blondeaux, P., 2000. Three-dimensional oscillatory flow over steep ripples. J. Fluid Mech. 412, 355–378.

Schielen, R.M.J., 1995. Nonlinear Stability Analysis and Pattern Formation in Morphological Models. Universiteit Utrecht, Faculteit Wiskunde en Informatica.

Sekiguchi, T., Sunamura, T., 2004. Effects of bed perturbation and velocity asymmetry on ripple initiation: wave-flume experiments. Coast. Eng. 50 (4), 231–239.

Shum, K.T., 1988. A Numerical Study of vortex Dynamics over Rigid Ripples. PhD thesis. Massachusetts Institute of Technology.

Sishah, B., Vittori, G., 2022. Ranse modeling of the oscillatory flow over two-dimensional rigid ripples. J. Geophys. Res. Oceans 127 (1) e2021JC017439.

Sleath, J.F.A., 1976. On rolling-grain ripples. J. Hydraul. Res. 14 (1), 69–81.

Sleath, J.F.A., 1984. Sea Bed Mechanics. John Wiley and Sons Inc., New York, NY.

Sleath, J.F.A., 1991. Velocities and shear stresses in wave-current flows. J. Geophys. Res. Oceans 96 (C8), 15237–15244.

Sleath, J.F.A., Ellis, A.C., 1978. Ripple Geometry in Oscillatory Flow. Cued/a-Hydraulics. Technical report, TR 2. University of Cambridge, Engineering Department.

Smith, P.A., Stansby, P.K., 1985. Wave-induced bed flows by a lagrangian vortex scheme. J. Comput. Phys. 60 (3), 489–516.

Soulsby, R.L., Whitehouse, R.J., 2005. Prediction of Ripple Properties in Shelf Seas. Mark 2 Predictor for Time Evolution. Technical report. HR Wallingford LTD Oxon (GREAT BRITAIN).

Soulsby, R.L., Whitehouse, R.J.S., Marten, K.V., 2012. Prediction of time-evolving sand ripples in shelf seas. Cont. Shelf Res. 38, 47–62.

Southard, John B., 1991. Experimental determination of bed-form stability. Annu. Rev. Earth Planet. Sci. 19 (1), 423–455.

Tanner, W.F., 1971. Numerical estimates of ancient waves, water depth and fetch. Sedimentology 16 (1–2), 71–88.

Tengberg, A., Almroth, E., Hall, P., 2003. Resuspension and its effects on organic carbon recycling and nutrient exchange in coastal sediments: in situ measurements using new experimental technology. J. Exp. Mar. Biol. Ecol. 285, 119–142.

Testik, F.Y., Voropayev, S.I., Fernando, H.J.S., 2005. Adjustment of sand ripples under changing water waves. Phys. Fluids 17 (7).

Tietze, K.W., 1979. Dynamik und sediment haushalt einer gezeitenlagune an der Nordseeküste der Bretagne. PhD thesis.

Vittori, G., 1989. Non-linear viscous oscillatory flow over a small amplitude wavy wall. J. Hydraul. Res. 27 (2), 267–280.

Vittori, G., Blondeaux, P., 1990. Sand ripples under sea waves. Part 2. Finite-amplitude development. J. Fluid Mech. 218, 19–39.

Vittori, G., Blondeaux, P., 1992. Sand ripples under sea waves. Part 3. Brick-pattern ripple formation. J. Fluid Mech. 239, 23–45.

Vittori, G., Blondeaux, P., 2022. Predicting offshore tidal bedforms using stability methods. Earth-Sci. Rev. 235 https://doi.org/10.1016/j.earscirev.2022.104234.

Vittori, G., Blondeaux, P., Mazzuoli, M., 2020a. Direct numerical simulations of the pulsating flow over a plane wall. J. Marine Sci. Eng. 8 (11), 893.

Vittori, G., Blondeaux, P., Mazzuoli, M., Simeonov, J., Calantoni, J., 2020b. Sediment transport under oscillatory flows. Int. J. Multiphase Flow 133.

Wilcox, D.C., 1988. Reassessment of the scale-determining equation for advanced turbulence models. AIAA J. 26 (11), 1299–1310.

Wilcox, D.C., 1993. Comparison of two-equation turbulence models for boundary layers with pressure gradient. AIAA J. 31 (8), 1414–1421.

Winters, K.B., Seim, H.E., Finnigan, T.D., 2000. Simulation of non-hydrostatic, density-stratified flow in irregular domains. Int. J. Numer. Methods Fluids 32 (3), 263–284.

Yoshikawa, H.N., Rousseaux, G., Kruithof, J., Stegner, A., Wesfreid, J.E., 2004. Flow structure over rolling-grain ripples–laboratory experiments and theoretical study. In: Marine Sandwave and River Dune Dynamics, pp. 346–351.

Zang, Y., Street, R.L., Koseff, J.R., 1993. A dynamic mixed subgrid-scale model and its application to turbulent recirculating flows. Phys. Fluids A 5 (12), 3186–3196.

Zedler, E.A., Street, R.L., 2006. Sediment transport over ripples in oscillatory flow. J. Hydraul. Eng. 132 (2), 180–193.